1   Interactions between buried mass-transport complexes and subsequent slope

2   failures on a passive margin

3   Nan Wu[1*], Christopher A.-L. Jackson[2], David M. Hodgson[3], Harya D. Nugraha[4,5], Guangfa Zhong[1]

4   [1]State Key Laboratory of Marine Geology, Tongji University, 1239 Siping Road, Shanghai, 200092, China
5   [2]Department of Earth Science and Engineering, Imperial College, Prince Consort Road, London, SW7 2BP,
6   UK
7   [3]School of Earth and Environment, University of Leeds, Leeds, LS2 9JT, UK
8   [4]Center for Sustainable Geoscience, Universitas Pertamina, Jakarta, 12220, Indonesia
9   [5]Department of Earth Science, University of Bergen, Allégaten 41, N-5007 Bergen, Norway
10   *nanwu@tongji.edu.cn

Abstract

12   Mass-transport complexes (MTCs) are common features on all continental margins, with

13   stacked MTCs indicating repeated slope failure. This suggests MTC generation and

14   emplacement may pre-condition a slope to fail again, although direct evidence for this is

15   currently lacking. Determining the relationship between MTC development and slope stability

16   is important, given its implications for understanding long-term basin evolution and geohazard

17   assessment. Here, we use 3D seismic reflection data from the Kangaroo Syncline, offshore NW

18   Australia, to investigate how preexisting MTCs can prime subsequent failure events. We

19   interpreted 11 MTCs that constitute approximately 80% of the total stratigraphic of the post-

20   Miocene interval, with individual MTC spanning areas of up to 2500 km². We show that: i)

21   lithological heterogeneity present within a sedimentary succession due to MTC emplacement

22   can impact the location of subsequent slope failures; ii) topography formed by a buried MTC

23   can enhance the erosive ability and effect the transport pathway of subsequent slope failure

24   events; iii) differential compaction between debrite matrix and blocks can produce a rugose

25   MTC top surface that can influence the distribution and stratigraphy of subsequent slope

26   failures; iv) the thickness pattern of buried MTCs can provide a mechanism for predicting the

depocentre of future slope failure events; and v) the nature of the sedimentary succession, the aseismic setting, the presence of fluid venting systems, and slope oversteepening can collectively contribute to the preconditioning of recurrent MTCs in the Kangaroo Syncline. Our results show that buried MTCs have profound effects on the location, nature, geometry, and hazard potential of future slope failures. Therefore, investigating the interaction between stacked MTCs is a crucial component of future geohazard impact assessments.

Keywords: Mass-transport complexes (MTCs), Exmouth Plateau, Geohazard assessment, Subaqueous slope failure, Subaqueous landsliding

1. Introduction

The term 'mass-transport complex' (MTC) is applied to a range of gravity-driven, subaqueous deposits resulting from creep, slide, slump, and debris flow processes (e.g. Dott Jr, 1963; Nardin et al., 1979; Nemec, 1990; Posamentier and Martinsen, 2011). MTCs can be very large (>10,000 km^3), and can travel quickly (>50 km/h) over long distances (i.e., >100 km), transporting large volumes of sediment, carbon, and nutrients from continental margins to the deep ocean (e.g., Talling et al., 2014; Kioka et al., 2019). The passage of an MTC can pose a great risk to submarine infrastructures (i.e. hydrocarbon- and windfarm-related platforms, and seabed cables), and generate powerful tsunamis that impact submarine ecosystems and threaten coastal populations (Harbitz et al., 2014; Talling et al., 2014; Lintern et al., 2019; Watkinson and Hall, 2019). The volumetrically largest MTCs on the planet occur on passive margins (Masson et al., 2006; Moscardelli and Wood, 2016). However, these large slope failure events are hard to predict, as they are primed and triggered by interacting factors including sea level fluctuations, climate change, substrate character and heterogeneity, sediment supply rates, and tectonic activity (Masson et al., 2010).

On some passive margins, slope failures are frequent, leading MTCs to be the most volumetrically dominant component of basin-fills, where 50%-90% are stacked MTCs (Appendix 1; Solheim et al., 2005; Sawyer et al., 2009; Li et al., 2015; Reis et al., 2016; Nugraha et al., 2018; Omeru and Cartwright, 2019; Steventon et al., 2019; Barrett et al., 2021). The morphology, distribution, kinematics, and priming and trigger mechanisms of some volumetrically significant MTCs, emplaced during a single event, have been considered, such as the Storegga Slide (i.e. Kvalstad et al., 2005), the Baiyun Slide (i.e. Sun et al., 2018), the Gorgon Slide (i.e. Nugraha et al., 2022), and the Amapá Megaslide Complex and Pará-Maranhão Megaslide Complex (i.e. Reis et al., 2016). However, few studies have investigated how preexisting MTCs influence subsequent slope failures in successions containing stacked MTCs, and even fewer have examined why slope failures in these sedimentary basins can recur over long geological timescales (Masson et al., 2006). Here, we investigate the interactions between eleven, post-late Miocene MTCs imaged in high-resolution 3D seismic reflection volume from the Kangaroo Syncline, offshore NW Australia. We seek to answer the following key questions: (i) why are MTCs abundant in the Kangaroo Syncline?; and (ii) what role do preexisting MTCs play in preconditioning the location, thickness, and volume of material removed, transported, and deposited during future slope failures?

2. Geological setting

The Kangaroo Syncline (or Trough) is a sub-basin of the North Carnarvon Basin, located on the NW Australian continental margin (Figure 1A; Hengesh et al., 2013; Scarselli et al., 2013a). As its name suggests, the Kangaroo Syncline is a c. 100 km-wide, NNE-trending, synclinal depocenter that is defined by a relatively low (0.08°-1.5°) seabed gradient (Hengesh et al., 2013). It is several hundred kilometres long and tens of kilometres wide, with present water depths of 1000-1300 m (Figure 1A; Exon et al., 1992; Hengesh et al., 2013). The Kangaroo Syncline formed in response to several rifting events that most recently occurred between the

75 Late Jurassic and Early Cretaceous (Longley et al., 2002). During the Late Cretaceous, uplift

76 of the Australian continental hinterland and structural inversion offshore on the southern

77 Exmouth Plateau led to the formation of the Kangaroo Syncline and Exmouth Plateau Arch

78 (Tindale et al., 1998). During the Late Oligocene, the Kangaroo Syncline and the Exmouth

79 Plateau Arch were reactivated due to the collision of the Australian and Eurasian plates (Barber,

80 1988; Keep et al., 1998; Cathro and Karner, 2006). Following that, in the late Miocene, the

81 collision of the Australian Plate with the Eurasia and Pacific plates led to further growth and

82 deepening, respectively, of the Exmouth Plateau Arch and Kangaroo Syncline (Tindale et al.,

83 1998). From the late Miocene to the Present, collision of the Australian Plate with the Eurasia

84 Plate accelerated tectonic subsidence of the Kangaroo Syncline and inverted rift-related faults

85 beneath the present continental shelf (Hull and Griffiths, 2002).

86 This study focuses on the late passive margin megasequence (late Miocene to Present). Water

87 depths at this time were bathyal (800-1500 m), with deposition dominated by eupelagic

88 carbonate (Exon et al., 1992; Haq et al., 1992). The study interval lies between Horizon 0 (H0,

89 approximately late Miocene) and the seabed (Figures 1B, 1C). Ocean Drilling Program (ODP)

90 Site 762 lies c. 270 km east of the study area near the apex of the Exmouth Plateau Arch, and

91 one industry well (Mercury-1) is located within the 3D seismic reflection survey (Figure 1A).

92 Core and geotechnical data from ODP site 762 and Mercury-1 indicate that the study interval

93 is dominated by highly compressible, low-velocity, water- and foraminifera-rich, carbonate

94 oozes (Figure 1B; Haq et al., 1992; Nugraha et al., 2018; Wu et al., 2023).

3. Dataset and methods

96 The primary dataset used in this study is the Willem 3D seismic reflection survey, acquired in

97 2011 (Figure 1A), which covers an 2628 km^2 area of the lower continental slope and adjacent

98 depocentre (i.e. the Kangaroo Syncline), in water depths of 200-1500 m (Figure 1A). The 3D

99   seismic reflection data were post-stack time-migrated (PSTM) and are displayed using SEG

100   reverse polarity, where a downward increase and decrease in acoustic impedance are expressed

101   as blue/black (negative) and red/white (positive) reflection events, respectively. The vertical

102   sampling rate of the seismic reflection data is 2 ms, and the bin size of the seismic survey is 25

103   x 25 m. From the seabed to the study interval, the dominant frequency of the 3D seismic

104   reflection data decreases from ca. 60 Hz to ca. 40 Hz, and the average seismic velocity increases

105   from 1750 m/s to 2000 m/s; we therefore estimate an approximate vertical resolution of 7.3 m

106   at the seabed, decreasing to 12.5 m near the base of the studied interval. The excellent spatial

107   resolution of the 3D seismic reflection data allows a detailed interpretation and characterization

108   of the MTCs' geometries, internal characteristics and emplacement directions.

109   The interval of interest (late Miocene-Recent; Figures 1B, 1C) correlates to seismic unit 3 of

110   Nugraha et al. (2018) and seismic unit 2 of Wu et al. (2023), who studied the seismic-

111   stratigraphy of adjacent areas. Previous studies indicate that the interval of interest contains

112   MTCs that either originated from the bathymetric highs of the lower NW Australian continental

113   slope, or the upper slope of the Exmouth Plateau Arch (Hengesh et al., 2012; Scarselli et al.,

114   2013a; Nugraha et al., 2018). Twenty-three seismic horizons (H0 to the seabed) have been

115   interpreted to define the base and top of each MTC, based on vertical and lateral changes in

116   seismic facies, the packages they define, and the expression of their bounding surfaces (Figures

117   2A, 2B). Variance and amplitude contrast attributes, as well as spectral decomposition (RGB

118   blending), have been extracted from the basal shear surface and the top surface of MTCs to

119   identify kinematic indicators that may reveal the MTC emplacement direction and

120   emplacement-related deformation. The variance attribute calculates the variability of a trace to

121   its neighbour over a particular sample interval and produces interpretable lateral changes in

122   acoustic impedance (Van Bemmel and Pepper, 2000). The amplitude contrast attribute

123   calculates the spatial gradient on an image; it improves the edge detection spatially and thereby

124 helps the identification of the terminations of the discontinuities (Aqrawi and Bø, 2016).

125 Spectral decomposition is a frequency-based seismic attribute that separates the seismic signal

126 into three frequency bands, including red (low frequency), green (mid frequency), and blue

127 (high frequency). When blended, this RGB visualization can help image structural and

128 stratigraphic features within MTCs (Partyka et al., 1999). Isochron (i.e. time-thickness) maps

129 of each MTC are computed from their basal and upper surfaces, with these being used to assess

130 the spatial relationships between subsequent MTCs. Finally, we calculate the dip, width and

131 incision depth of grooves, formed by the dragging of rigid blocks contained at the base of slope

132 failures to quantify the flow direction and the erosional capacity of the MTCs during their

133 emplacement (Bull et al., 2009; Sobiesiak et al., 2018).

134 4. Results

135 This study focuses on eleven stacked MTCs (MTC 1-11) that comprise nearly 80% of the

136 stratigraphic thickness of the studied stratigraphic interval (Figures 2A, 2B; Table 1). The

137 eleven studied MTCs are characterised by packages of chaotic, variable-amplitude reflections

138 (cf. Bull et al., 2009; Posamentier and Martinsen, 2011). They are bound below by a positive

139 polarity, high-amplitude, continuous basal shear surfaces, and above by a medium-amplitude,

140 negative polarity, rugose top surface. In the following section we describe the distribution,

141 external and internal geometry, emplacement direction and kinematics of the 11 MTCs, from

142 oldest (MTC-1) to youngest (MTC-11).

143 4.1 MTC-1

144 *Description:* MTC-1 is internally chaotic and defined at its base and top by H1 and H2,

145 respectively (Figures 2A, 2B). A variance attribute calculated within H1 indicates a tongue-

146 shaped geometry, narrowing to the NNE (Figures 3A, 3B). The western boundary of MTC-1

147 is defined by an NE-trending erosional margin associated with a younger MTC (MTC-2),

148   whereas its eastern boundary trends N-S and is defined by an erosion surface defining the base

149   of another younger MTC (MTC-4) (Figures 3A, 3B). Below the middle of MTC-1, NNW-

150   trending lateral ramps and E-trending internal ramps are present, with numerous NNE-trending,

151   diverging lineations observable beyond the internal ramp (Figure 3B). MTC-1 is overlain by

152   approximately 300 m of slope deposits and is eroded by later MTC-2 in its western part (Figure

153   3C). MTC-1 thins to the northeast, and its basal shear surface dips north-northeastward (Figure

154   3D).

155   ***Interpretation:*** The geometry of MTC-1 is an erosional remnant of its original distribution,

156   due to the later incision by MTC-2 (i.e. in the west) and MTC-4 (i.e. in the east) (Figure 3B);

157   it is thus likely that MTC-1 initially extended further westwards and eastwards. The seismic

158   expression of the predominantly chaotic reflections is typical of an internally highly deformed

159   debrite, similar to other drilled examples of MTCs (Piper et al., 1997). The lineations developed

160   beyond the internal ramp are interpreted as basal grooves (i.e. Posamentier and Martinsen, 2011;

161   Sobiesiak et al., 2018), formed by clasts carried within the host flows that scoured the

162   contemporaneous seabed. Grooves typically form parallel to the MTC transport direction,

163   which together with the NNE downward trending of the basal shear surface, suggest MTC-1

164   was emplaced towards the NNE (Gee et al., 2005; Bull et al., 2009). Internal and lateral ramps

165   result from MTCs cutting up through stratigraphic levels, creating a step-like geometry in

166   cross-section (Frey-Martínez et al., 2006; Bull et al., 2009). The lateral and internal ramps are

167   considered to trend parallel and perpendicular to the MTCs' transport direction, respectively

168   (Bull et al., 2009). We therefore interpret a NNE translation direction for MTC-1, consistent

169   with that inferred from the grooves (Figure 3B).

170   **4.2 MTC-2**

171 ***Description:*** MTC-2 is defined at its base by H3 and its top by H4 (Figures 2A, 2B). A variance

172 attribute calculated within H3 indicates MTC-2 has a semi-elliptic geometry, with its eastern

173 boundary defined by a NE-trending headwall scarp and its western boundary by an erosional

174 ramp associated with the younger MTC-3 (Figures 4A, 4B). The isochron of MTC-2 reveals

175 that it thins westward from its headwall (Figure 4C). The variance attribute indicates that MTC-

176 2 contains numerous parallel to sub-parallel, block-shaped packages in its eastern part (Figures

177 4A, 4B). In seismic sections, these form ridge-shaped blocks flanked by troughs (Figure 4D).

178 The blocks are 210-300 m high, 170-210 wide, and 800-1,200 m long, with minor internal

179 deformation (Figure 3C, 4D). The intervening troughs are 160-260 m deep, 190-230 m wide,

180 800-1,200 m long and are defined by a chaotic, variable-amplitude seismic facies (Figure 4D).

181 The lower section of the blocks is characterized by chaotic seismic facies, comparable to those

182 characterising the entirety of MTC-1 (Figure 3C, 4D). The chaotic seismic facies are also

183 bound by medium to high-amplitude, positive reflections, comparable to those bounding MTC-

184 1 (Figure 3C). The blocks decrease in size, lose their block-shaped form, and become internally

185 more deformed westwards (Figure 4D).

186 ***Interpretation:*** MTC-2 was previously described by Wu et al. (2021b), who document a c. 300

187 m thick succession of undeformed slope strata between MTC-1 and MTC-2 (Figure 4D).

188 Unlike MTC-1, the basal shear surface of MTC-2 lacks kinematic features (i.e. lateral margins,

189 ramps, or grooves; Figure 4A) that record its emplacement direction. Despite this, Wu et al.

190 (2021b) interpret a north-northwestward translation direction, along the axis of the Kangaroo

191 Syncline, based on its headwall scarp orientation (i.e., NE-SW) and spatial trends in block size

192 (i.e. blocks decrease in size towards the WNW) (Figure 4B; Wu et al., 2021b). Based on their

193 geometric characteristics and distribution, the intra-MTC blocks are interpreted as being related

194 to lateral spreading (Wu et al., 2021b). The similarity in the seismic facies characterising the

195 intra-MTC blocks and the undeformed strata (i.e. a thin MTC overlain by largely undeformed

strata) suggests the former are derived from the latter (Figures 3C, 4D). This is supported by the observations that the blocks in the eastern part of MTC 2 are the same thickness as the laterally adjacent, largely undeformed slope succession (Figures 3C). We therefore interpret that the emplacement of MTC-2 led to erosion of the underlying MTC-1, with portions of MTC-1 being entrained into and forming part of the basal shear zone of MTC-2.

4.3 MTC-3

Description: MTC-3 overlies MTC-2, separated by a c. 30 m package of slope deposits. It is bounded by H5 and H6 at its base and top, respectively (Figures 2A, 2B). The variance attribute calculated from H5 reveals that MTC-3 has a scallop-shaped geometry in plan-view (Figures 5A, 5B). The eastern boundary of MTC-3 is defined by an NNE-trending scarp, whereas its western boundary is beyond the 3D seismic reflection dataset (Figure 5B). The isochron of MTC-3 shows that it thins eastward, showing an opposing thickness trend to MTC-2 (Figure 5C).

A seismic section through MTC-3 reveals that it comprises blocky seismic facies in the west, chaotic seismic facies near its centre, and semi-continuous, medium-amplitude seismic reflections offset by thrusts faults in the east (Figure 4D). The central region of MTC-3 contains several E to SE trending linear features that are least 7 km long (Figures 5A, 5B). A seismic section shows that the linear features are up to 400 m wide and 60 m deep, and have a U-shaped geometry that truncate underlying reflections (Figure 5D). The eastern region contains numerous broadly eastward-convex, regularly spaced undulations, with the eastern, most distal part of MTC-3, notably coinciding with where the underlying lateral spreads (associated with MTC-2) are developed (Figures 5B, 5E). In detail, the regularly spaced undulations are characterised by semi-continuous, medium-amplitude seismic facies that terminate against the

219 relief created by the underlying lateral spreads (Figure 5E). Further east, the seismic reflections

220 are continuous and drape the lateral spreads, defining low-relief folds (Figure 5E).

221 *Interpretation:* The NNE-trending eastern boundary is interpreted as the distal limit of MTC-

222 3, where the deposit changes from principally debritic material to undeformed, slope sediments

223 (Figures 5A, 5B). The linear features at the base of MTC-3 in the west of the seismic survey

224 are interpreted as erosional scours (i.e. Moscardelli et al., 2006), which potentially formed by

225 the sliding or dragging of blocks across the substrate as the MTC was emplaced (Gee et al.,

226 2005; Sobiesiak et al., 2018). The regularly spaced undulations near the eastern boundary of

227 MTC-3 are interpreted as pressure ridges caused by compression or horizontal shortening of

228 transported material, noting that such features are normally convex in the downslope direction

229 (Nissen et al., 1999; Bull et al., 2009). The pressure ridges are underlain by, and likely

230 genetically related to, thrusts, suggesting the failed mass remained frontally confined (Figure

231 5E; Frey-Martínez et al., 2006). Pressure ridges and scours normally develop perpendicular

232 and parallel to an MTC's main flow direction, respectively (Bull et al., 2009). We therefore

233 interpret that the transport direction of MTC-3 was towards the east and south-east (Figure 5B).

234 The lateral spreads associated with MTC-2 developed considerable positive relief of a few tens

235 of metres overall several kilometres horizontally; we infer frontal buttressing of MTC-3 relief

236 caused shortening and thrusting in its distal part (Figure 5E). MTC-2 and MTC-3 show

237 opposing emplacement directions and thickness trends (Figures 4C, 5C), suggesting that relief

238 associated with the former controlled the bathymetric template onto which the latter was

239 emplaced. After deposition of MTC-3, the paleo-seabed began to heal via the deposition of

240 fine-grained carbonate oozes that drape the top surface of MTC-3 (Figure 5E; Nugraha et al.,

241 2018).

242 **4.4 MTC-4 & MTC-5**

243   ***Description:*** MTC-4 is located c. 30 km east of MTC-3, with its base defined by H7 and its

244   top by H8 (Figures 2A, 2B). The variance attribute analysis derived from H7 demonstrates that

245   MTC-4 exhibits a lobate geometry in plan-view (Figure 6A). The eastern and western

246   boundaries of MTC-4 are defined by N and NNW-trending lateral scarps. Spectral

247   decomposition attributes reveal that the distal part of MTC-4 is characterized by fingerprint-

248   like structures, consisting of curved lineations that are convex downslope to the north, offset

249   by NNW-trending longitudinal lineations, oriented perpendicular to the fingerprint-like

250   lineations (Figures 6B, 6C). Seismic section across MTC-4 reveals chaotic, highly

251   discontinuous, medium-amplitude reflections at its updip end (southeastern part), transitioning

252   to isolated, folded, high-amplitude reflections encased within chaotic, transparent reflections

253   near the proximal part. In the downdip part it comprises pairs of high-amplitude, high-angle

254   discontinuities that converge downward onto the basal shear surface (Figure 6D).

255   MTC-5 overlies MTC-4, separated by c. 30-50 m thick slope deposits, and is bounded by H9

256   at its base and H10 at its top (Figures 2A, 2B). Variance attribute analysis extracted from H9

257   reveals that MTC-5 is characterized by NNE-trending updip and distal margins, as well as a

258   NNW-trending northern lateral margin (Figure 7A). Like MTC-4, the proximal and distal parts

259   of MTC-5 exhibit fingerprint-like structures with a convex-downslope geometry, characterized

260   by lineations overall striking NNE–SSW (Figures 7B, 7C). The distal morphology of MTC-5

261   is characterized by multiple lobate features that exhibit cross-cutting relationships, and which

262   are bounded by NNW-trending, longitudinal margins (Figure 7B). Internal lineations are more

263   intensely deformed close to these margins. Seismic section reveals that the basal shear surface

264   of MTC-5 incises multiple stratigraphic levels and is associated with variable internal seismic

265   facies. For example, in the updip region of MTC-5 is dominated by chaotic reflections, whereas

266   the proximal region is characterised by high-amplitude, high-angle discontinuities that cut

267   upward from the basal shear surface (Figure 7D). The distal region is dominated by thrust-

268 bounded blocks that preserve coherent stratigraphy, whereas the intervening zones exhibit

269 disrupted reflections or acoustically chaotic facies. Further downslope, the basal shear surface

270 steps upward into shallower stratigraphic levels, where it is overlain by steeply dipping, closely

271 spaced faults (Figure 7D).

272 ***Interpretation:*** The N and NNE-trending scarps flanking MTC-4 are interpreted as its lateral

273 margins; their trend suggests the deposit was transported broadly northwards (Bull et al., 2009)

274 (Figure 6C). The continuous lineations that are deformed into curvilinear, fingerprint-like

275 structures in map view, and which correspond to reflection discontinuities in the seismic

276 section, are interpreted as forethrusts and back-thrusts uplift internally coherent pop-up blocks

277 (Nugraha et al., 2020). The high-angle discontinuities are interpreted as contractional thrusts

278 that commonly accommodate a major portion of the total downslope shortening (Frey-Martínez

279 et al., 2006). The longitudinal lineations perpendicular to the strike of the fingerprint-like

280 structures are interpreted as longitudinal shear zones, which form due to velocity contrasts

281 between adjacent flow compartments during MTC emplacement (Steventon et al., 2019;

282 Nugraha et al., 2020; Abu et al., 2022).

283 The NNE-trending updip and downdip margins of MTC-5 are interpreted as the headwall scarp

284 and distal margin, respectively (Figure 7C), marking the boundary between the deformed

285 region and the surrounding undeformed slope (Bull et al., 2009). Similar to MTC-4, the

286 fingerprint-like structures are interpreted as compression-related features, whereas the cross-

287 cutting lobes are considered to represent discrete flow cells that accommodate across-strike

288 variations in the total magnitude of down-dip transport, bounded by longitudinal shear zones

289 (Steventon et al., 2019; Nugraha et al., 2020). The chaotic reflections are interpreted as debrite,

290 the high-amplitude, high-angle discontinuities as contractional thrusts, and the thrust-bounded

291 blocks as pop-up structures. In both MTC-4 and MTC-5, the along-strike transition from

292 chaotic debrite to well-defined pop-up blocks and thrusts reflects progressive frontal

293 compression during the final stages of emplacement. This structural complexity is influenced

294 by factors such as frontal confinement (buttressed vs. emergent runout), internal flow

295 compartmentalization, and multi-phase deformation, all of which contribute to and record the

296 complex kinematic interactions and strains at the front of an MTC as it stops (Abu et al., 2022).

4.5 MTC-6 & MTC-7

298 *Description:* MTC-6 is separated from MTC-5 by an 80 -160 m thick package of slope deposits

299 in the eastern part of the study area, and is bounded by H11 at its base and H12 at its top

300 (Figures 2A, 2B). A variance attribute map reveals MTC-6 has a W- to SW-trending southern

301 margin and a N- to NE-trending distal margin (Figures 8A, 8B). The basal shear surface of

302 MTC-6 is locally defined by a broadly NNW-trending continuous scarp that is flanked by two

303 sets of lineations. South of the scarp, the lineations trend NNW whereas to the north they trend

304 a NW. MTC-6 is mainly composed of chaotic seismic facies, underlain by a high-amplitude,

305 positive-polarity basal shear surface (Figure 8E). The basal shear surface extends further

306 upslope, where it serves as the basal boundary for multiple younger MTCs (i.e., MTC-7, MTC-

307 8 and MTC-9; see below).

308 MTC-7 is deposited directly above MTC-6, being bounded by H13 at its base and H14 at its

309 top (Figure 8E). The variance attribute map extracted through MTC-7 reveals it is bounded by

310 a NNE-trending margin defining its updip extent, and a NNW-trending margin delineating its

311 downdip extent. The southwestern part of MTC-7 is partially incised by the subsequent MTC-

312 8 (Figures 8C, 8D). Internally, MTC-7 contains NNW-trending lineations in its proximal part,

313 a concave-downward, semi-enclosed scarp in its southeastern part, and a NNW-trending scarp

314 in its northeastern part. Seismic sections reveal that this MTC is internally chaotic, with its

315 basal shear surface partially merging with that of the underlying MTC-6 in the shared headwall

316 region (Figure 8E).

Interpretation: The W- to SW-trending southern boundary of MTC-6 is interpreted as the lateral margin of the deposit, whereas the N-trending represents its distal margin (Bull et al., 2009). The NNW-trending basal lineations of MTC-6 are interpreted as grooves. Accordingly, we interpret that the MTC-6 was emplaced toward the NNW, parallel to the dip direction of the grooves. The NNW-trending continuous scarp is interpreted as an internal ramp, where the basal shear surface stepped upward into shallower strata during emplacement, resulting in a shift of groove orientation from NNW-SSE to NW–SE.

The NNE-trending margins that define the updip and downdip extents of MTC-7 are interpreted as the headwall scarp and distal margin, respectively. The NNW-trending lineations are interpreted as basal grooves, whereas the NNW-trending scarp is interpreted as an internal ramp. Based on the orientation of the headwall scarp and basal grooves, we interpret the transport direction of this MTC was towards the NNW. The partially overlapping basal shear surfaces indicate that during its emplacement, MTC-7 eroded into the underlying MTC-6 in the headwall region, causing the basal shear surfaces of the two MTCs to merge. This, in turn, suggests that the basal shear surface of the buried MTC-6 locally influenced the maximum erosion depth of the subsequent slope failure.

4.6 MTC-8

Description: MTC-8 directly overlies MTC-7 in the eastern part of the study area, whereas it is separated from MTC-3 by a 30-70 m thick package of slope deposits in the western part (Figures 2A, 2B). MTC-8 is bounded by H15 at its base and by H16 at its top (Figure 8E). The amplitude contrast attribute extracted from the BSS of MTC-8 (H15) is characterized by a NW-trending lateral margin on its northeastern side and NW-oriented internal ramp structures within its central region (Figures 9A-9C). The isochron of MTC-8 shows it is thinnest in its middle and thickest in its western and eastern portions (Figure 9D). Curvilinear lineations are

341 observed on the basal shear surface beneath both the northeastern and southwestern regions of

342 MTC-8 (Figures 9B, 9C). In the northeastern region, these sub-parallel lineations extend for

343 30-50 km in a NW-direction. Seismic sections reveal that the lineations are erosional,

344 containing block-shaped packages incised into the BSS and underlying relief capping MTC-7,

345 and delineating a prominent channel-like geometry on the basal shear surface (Figure 10A).

346 These block-shaped packages are 80-220 ms (approximately 60-150 m) in thick and 700-1100

347 m wide. Internally, they are characterized by highly deformed to transparent reflections, exhibit

348 angular to sub-angular morphologies, and are embedded within a seismically chaotic matrix

349 (Figure 10A). In its central region, the basal shear surface exhibits a finger-like protruding

350 structure, characterized by short, NNE-trending lineations (Figure 10B). These lineations

351 correspond to high-amplitude, discontinuities or folded, and steeply dipping reflections

352 observed in seismic section (Figure 10C). Additionally, this finger-like, protruding structure

353 occurs directly above MTC-7, with the internal steeply dipping reflections terminating against

354 it (Figure 10C).

355 In the southwestern region, where MTC-8 caps MTC-3, MTC-8 is locally thick where the

356 underlying MTC-3 is thin, and vice versa (Figure 9D). In this region, the lineations are 20-40

357 km long and show a radial distribution pattern (Figures 9B, 9C, 11A). The lineations are

358 erosional, defining a prominent V-shaped geometry, and are 12-50 ms deep and 50-300 m wide

359 (Figures 9D). The terminations of the lineations exhibit a semi-elliptical morphology, within

360 which the seismic data reveal rounded edges and angular blocks (Figure 11A). In the same area,

361 we observe that the NW-trending internal ramp on the basal shear surface is superimposed

362 above the headwall scarp of the buried MTC-2 (Figures 9D, 11A). The NE-trending internal

363 ramp along the BSS of MTC-8 separates lineations of two different trends (Figures 11A). To

364 the SE of the internal ramp, they trend NW to NNW (315-330º), whereas to the NW of the

365 internal ramp they trend NNE to NE (015-045º), broadly parallel to the axis of the Kangaroo

366   Syncline (Figures 11D). Additionally, the lineations exhibit a V-shaped geometry southeast of

367   the internal ramp, transitioning to U-shaped profiles northwest of it (Figure 12). To assess how

368   erosion varies across the NE-trending internal ramp, we pick one of the most continuous

369   lineations (G-1; Figure 11A) to quantify down-trend variations in its width and depth. From

370   the SE to the NW of the internal ramp, the width and erosion depth of G-1 increases sharply

371   from 110 to 270 m and 18 to 45 ms, respectively (Figure 11E).

372   *Interpretation:* The block-shaped features associated with the scours and high relief on the top

373   surface in the northeastern region of MTC-8 are interpreted as megaclasts (Figure 10A). These

374   are large clasts ranging from hundreds of meters to kilometers in diameter, transported within

375   MTCs (Jackson, 2011; Hodgson et al., 2018). The transparent internal reflections and angular

376   to sub-angular morphologies, suggesting they were well-consolidated prior to entrainment

377   (Hodgson et al., 2018). Interaction between these megaclasts and the underlying substrate

378   generated deep erosional scours into the substrate, thereby modifying the morphology of the

379   basal shear surface and deforming MTC-7.

380   In the central region of MTC-8, the lineations within the finger-like protruding structure are

381   interpreted as fold-and-thrust belts formed during compression towards the toe domain of the

382   MTC (Figures 10B, 10C; Steventon et al., 2019). Given that these features spatially overlap

383   with remnant relief above the underlying MTC-7, we suggest that this relief caused the

384   deceleration of, and compression and shortening within, the subsequent mass flow (e.g., Figure

385   10C).

386   The curvilinear lineations developed in the northwestern region are interpreted as grooves

387   (Posamentier and Kolla, 2003; Gee et al., 2005). The observation of clasts within the grooves

388   supports that they were transported at the base of the debris flow and acted as erosional tools

389   during submarine landsliding (Peakall et al., 2020; Figure 11C). Therefore, the variation in

390 orientation, cross-sectional geometry, and scale of grooves across the NE-trending internal

391 ramp suggests flow divergence during the emplacement of MTC-8. The presence of the NE-

392 trending internal ramp corresponds to an area where MTC-8 incised into deeper stratigraphy

393 and thickened as a result (Figures 9E, 11A). The thickness change in MTC-8 across the internal

394 ramp reflects the thickness pattern of MTC-3, where unhealed relief remained near the

395 headwall of MTC-2 (Figure 9E).

396 The groove trend along the BSS of MTC-8 suggests it was steered away by the NE-trending

397 internal ramp from a shallower area in the SE and cut down to be more confined to the NW

398 (Figures 11A, 12). The grooves are wider and deeper to the NW, suggesting either larger

399 megaclasts are entrained from the ramp, or given the continuity of grooves, that the megaclasts

400 were able to gouge deeper into the substrate (Figure 11). The thickness of MTC-8 thus increases

401 in the area of the MTC-2 and 3 headwall resulting the generation in a downstream-facing ramp

402 (Figures 9A, 9D). Therefore, we suggest that MTC-2 and 3 controlled local seabed topography

403 that influenced the emplacement of MTC-8, enhancing its erosive ability, diverting its flow

404 direction, and providing a focal point for its ultimate deposition.

405 **4.7 MTC-9**

406 *Description:* MTC-9 directly overlies MTC-8 and is bounded by H17 at its base and by H18 at

407 its top (Figure 8E). The amplitude contrast attribute calculated on H17, the BSS of MTC-9,

408 reveals that the overlying deposit is the most aerially extensive in the study area (at least 2500

409 km^2; Figures 13A, 13B). The isochron of MTC-9 displays a tripartite thickness distribution,

410 being thickest in the NW and SE portions, and thinner in-between (Figure 13C). MTC-9 is

411 bounded updip by an NE-trending scarp located in the southeastern part of the study area that

412 separates the internally deformed area from the undeformed substrate. Several asymmetrical,

413 sparsely distributed blocks are observed to the NW of this scarp and in the northeastern region

414 (Figures 13A, 13B). The presence of these blocks results in a rugose top surface of MTC-9,

415 exhibiting localized topographic highs (Figure 13D).

416 Based on their internal deformation intensity and external geometry, three distinct block types

417 are identified: (i) highly deformed blocks, up to 300 m diameter and 180 m thick, that are

418 located in the proximal region and associated with NNW-trending lineations that incise the

419 underlying substrate by several tens of meters and cone-shaped ridges of the underlying deposit

420 (Figures 14A, 14B). These blocks are characterized by chaotic to transparent internal

421 reflections, with angular to sub-angular terminations at their top surface (Figures 14C, 14D).

422 (ii) moderately deformed blocks, up to 2.7 km diameter and nearly 300 m thick, located near

423 the headwall region, and as such, inferred to have remained relatively in-situ during MTC

424 emplacement (Figure 15A). These blocks are characterized by semi-continuous, faulted and

425 folded internal reflections, have rounded to sub-rounded external geometries, and rest on a

426 planar basal surface (Figures 15B, 15C). Seismic reflections overlying these blocks exhibit

427 clear onlap terminations onto the top surface of the MTC-9, with seismic reflections draping

428 against both flanks of the topographic highs (Figure 15B). The lower part of these blocks,

429 corresponding to the basal shear surface, is typically marked by deformed to chaotic seismic

430 reflections (Figure 15C); and (iii) tabular shaped blocks, located near the MTC proximal region.

431 The long axes of these blocks trend NW and are up c. 17 km long (Figures 13A, 13B). These

432 blocks are internally defined by undeformed, continuous reflections that are abruptly bounded

433 by chaotic seismic reflections characterising the main body of MTC-9 (Figure 15D). No visible

434 basal deformation is observed directly beneath the in-situ blocks (Figure 15D).

435 ***Interpretation:*** We interpret the lineations in MTC-9 as emplacement-related scours and the

436 headwall scarp. The location of the headwall scarp defines the source area of the slope failures

437 (Bull et al., 2009; Posamentier and Martinsen, 2011); thus, given the headwall scarp of the

438 MTC-9 is located on the lower continental slope, we infer it was sourced from here and

439 transported northwestward. This interpretation is consistent with the NW-SE trend of the basal

440 scours (Figure 13B). The moderately deformed blocks developed near the headwall scarp are

441 interpreted as transported blocks representing relatively competent pieces of failed material

442 that have been transported within the MTC (Figures 15A, 15B; i.e. Frey Martinez et al., 2005;

443 Bull et al., 2009). The highly deformed blocks developed in the eastern part of MTC-9 are

444 interpreted as megaclasts, representing failed material that were rotated during transport and

445 travelled a relatively long distance (Figures 14C, 14D; Nwoko et al., 2020). The internally

446 undisturbed block is interpreted as a remnant block of substrate surrounded by failed and

447 transported material within the main MTC body (Figure 15D; i.e. Frey Martinez et al., 2005;

448 Bull et al., 2009).

449 The megaclasts and transported blocks are sufficiently thick to remain unburied by MTC-9,

450 protruding above the top surface and even the modern seabed, as evidenced by the onlap of

451 younger sediments against their flanks (Figures 14C, 14D, 15B, 15C). Given their substantial

452 thickness, the transported blocks and megaclasts likely originated from the headwall region

453 and are interpreted to have been entrained and carried downslope within the debris flow during

454 transport. Localized uplifted topography, exceeding 120 m in relief, formed a series of

455 seamount-like structures on the paleo-seabed, which continue to influence modern seabed

456 morphology (Figures 14D, 15B, and 15C). These features act as barriers to subsequent MTC-

457 10 and MTC-11.

4.8 MTC-10 & MTC-11

459 *Description:* MTC-10 directly overlies MTC-9, with its base and top defined by H19 and H20,

460 respectively (Figure 14C). MTC-10 broadly trends NW, is confined to the NE part of the study

461 area, and has a tabular geometry in plain view (Figures 16A). The eastern and western

462 boundaries of MTC-10 are characterized by NW-trending margins (Figure 16A). The isochron

463   of MTC-10 reveals it is thick in areas where the underlying MTC-9 is thin, and thin or absent

464   where the underlying MTC-9 is thick (Figures 13C, 16B). The seismic section of MTC-10

465   consists of a package of chaotic seismic facies that pinches out toward the local topographic

466   high associated with positive relief along the upper surface of MTC-9 (Figure 17A).

467   MTC-11, overlies MTC-10, with its base and top defined by H21 and seabed, respectively

468   (Figure 17A). Like MTC-10, MTC-11 trends NW and is confined to the northeastern part of

469   the study area (Figures 16C, 16D). It exhibits a tongue-shaped geometry characterized by two

470   distinct lobate forms in the northwest. The eastern and western boundaries of MTC-11 are

471   defined by NW-trending margins that parallel to those of the underlying MTC-10 (Figures 16C,

472   16D). The isochron map of MTC-11 indicates that it is thick in areas where the underlying

473   MTC-9 is thin, and conversely, thin or absent where MTC-9 is thick (Figure 16D). In a similar

474   manner to MTC-10, MTC-11 is internally chaotic and thins and pinches out toward the local

475   topographic high associated with positive relief along the upper surface of the underlying

476   MTC-9 (Figures 16E). MTC-11 is obstructed and frontally confined by topographic barriers

477   formed by preexisting blocks within the underlying MTC-9, resulting in a relatively short run-

478   out distance of approximately 23–30 km (Figure 17B). In contrast, where the underlying blocks

479   are absent, MTC-11 overrides the existing seabed topography extends downslope beyond the

480   limits of the 3D seismic dataset (Figure 17C).

481   *Interpretation:* The NW-trending margins associated with MTC-10 and MTC-11 are

482   interpreted as their lateral margins (Figure 16A). Based on the trend of these lateral margins,

483   we interpret that MTC-10 and MTC-11 were emplaced towards the NW. The depocenters of

484   MTC-10 and MTC-11 overlap spatially above the thinner sections of the underlying MTC-9,

485   suggesting that the seafloor relief created by MTC-9 influenced the deposition of the former

486   two deposits (Figure 16E). The central part of MTC-11 is classified as frontally confined, given

487   it is characterised by an abrupt frontal termination (Frey-Martínez et al., 2006). This

confinement results from pre-existing topographic barriers formed by blocks within the underlying MTC-9, which impeded further downslope translation. In contrast, the lobate regions of MTC-11 represent frontally emergent domains, where the MTC seemingly overrode subtle seabed relief and propagated freely downslope, resulting in a longer runout distance. These contrasting frontal styles highlight the complex and spatially heterogeneous emplacement dynamics of MTC-11 (Nugraha et al., 2020).

5. Discussion

We show that the post-Miocene succession of the Kangaroo Syncline is dominated by stacked MTCs. In this section we consider the potential controls on the relative abundance of MTCs in the Kangaroo Syncline, discuss how earlier MTCs can influence the location and scale of subsequent slope failures, and consider the implication of our results for predicting the future occurrence of MTCs and related geohazards and mitigating their impacts.

5.1 Why was MTC emplacement common in the Kangaroo Syncline during the Neogene?

The interplay of factors controlling recurrent submarine landslides along passive margins, where the intensity and frequency of tectonic deformation and seismic activity are substantially lower than those of active margins, remain poorly understood. In the Kangaroo Syncline, the stacked MTCs indicates it has been a major depocenter for material originating from adjacent slope failures, which potential pose geohazard risks to existing and planned subaqueous infrastructure offshore NW Australia (Piper et al., 1999; Hengesh et al., 2012; Gavey et al., 2017; Pope et al., 2017). Therefore, investigating the controlling factors for recurrent slope failure within the Kangaroo Syncline provides insight that are applicable to other MTC-rich sedimentary systems on passive margins worldwide.

5.1.1 Sediment Properties and their Role in Slope Failure

512 In the Kangaroo Syncline, carbonate ooze, which consist of foraminifera and other nannofossils,

513 has been the dominant sediment deposit since the late Miocene (Nugraha et al., 2018).

514 Carbonate oozes are highly compressible and have distinct geotechnical characteristics,

515 including high water content (i.e. >50%), low permeability, and low shear strength compared

516 to fine-grained siliciclastic sediments (von Rad, 1992; Urlaub et al., 2015; Gatter et al., 2021).

517 The continuous deposition of carbonate oozes can result in sudden dewatering that causes an

518 increase in sediment pore pressure, resulting in a sufficient excess pore pressure to precondition

519 a low-gradient slope to fail (e.g. Tanaka and Locat, 1999; Volpi et al., 2003; Davies and Clark,

520 2006). Furthermore, the amount of water stored within shell chambers and skeletal pores in

521 ooze can be as high as 15% of their dry weight (Palmer-Julson and Rack, 1992; Rack et al.,

522 1993). The crushing of fragile biogenic particles could lead to further expulsion of intraparticle

523 water (Urlaub et al., 2015). Laboratory experiments suggest that carbonate oozes are more

524 susceptible to failure than siliciclastic sediments (Gaudin and White, 2009). During the shear

525 strength cyclic T-bar test of carbonate oozes and siliciclastic sediments, the residual shear

526 strength of carbonate oozes drops rapidly to only 10% of their initial strength, whereas the

527 residual strength of siliciclastic sediments can be up to 55% of their initial strength (Figure

528 18A; Gaudin and White, 2009). Consequently, carbonate oozes lose shear strength rapidly

529 when their strain-bearing capacity is exceeded. This property may explain why slope failures

530 occur frequently in carbonate ooze-rich settings, even on very gently dipping slopes

531 characterised by low rates of sediment accumulation, such as the Kangaroo Syncline. However,

532 the exact failure mechanisms require investigation through drilling derived physical properties

533 before and after failure.

534 The northwest Norwegian continental margin exhibits similar sedimentological and

535 geotechnical properties, with slope failure and the emplacement of large MTCs repeatedly

536 occurring during the Quaternary, at intervals of approximately 100,000 years (Bryn et al., 2005;

537   Solheim et al., 2005). Sediments in this region, particularly fine-grained biogenic marine oozes

538   interbedded with glaciogenic deposits, are characterized by exceptionally high water content

539   (70% to 90%; Lawrence and Cartwright, 2010; Bellwald et al., 2024). The result is sediments

540   with extremely low bulk densities and high compressibility (Bellwald et al., 2024). Such

541   sedimentological properties enhance pore-pressure accumulation and markedly reduce

542   sediment shear strength, providing ideal conditions for slope instability (Kvalstad et al., 2005).

543   Consequently, these fine-grained, high-water-content sediments inherently predispose slopes

544   along the Norwegian margin to recurrent, large-scale submarine slope failures, in a similar way

545   to the Kangaroo Syncline.

546   *5.1.2 Fluid Venting System and Vertical Fluid Migration*

547   Excess pressures generated by fluid and/or gas migration may precondition a slope to fail (Bünz

548   et al., 2005; Berndt et al., 2012), with this also being true for the Kangaroo Syncline (Wu et al.,

549   2023). In the latter case, excess pore pressure had, and possibly still has, two sources. First,

550   silica diageneses (opal-A to opal-CT conversion) during the burial of the Eocene, chalk-rich

551   succession, which led to fluid expulsion and overpressure development (Wu et al., 2023). A

552   similar mechanism is proposed for a submarine landslide in the Faroe-Shetland Channel, NW

553   offshore UK (Davies and Clark, 2006). Second, gas was likely migrating from the

554   hydrocarbon-bearing Mungaroo Formation (Triassic) during the Neogene, again leading to

555   overpressure development in the shallower stratigraphy (Paganoni et al., 2019; Velayatham et

556   al., 2019). A similar priming mechanism has been identified offshore Norway, in this case in

557   association with gas hydrate dissociation and migration from beneath the main headwall of the

558   Storegga Slide (Sultan et al., 2003; Strout and Tjelta, 2005). Similar fluid migration processes

559   have also been proposed as key preconditioning factors for slope instability in other regions,

560   including the Baiyun Slide complexes in the South China Sea (Li et al., 2014) and the stacked

561   MTCs in the Taranaki Basin, offshore New Zealand (Ilg et al., 2012). Therefore, sedimentary

562   basins characterised by widespread, sustained, and more importantly, focused gas or fluid

563   generation and migration pose higher risk of slope failure, such as in Kangaroo Syncline.

564   *5.1.3 The Relationship Between Seismicity and Sediment Properties*

565   Although the collision between the Australian and Eurasian plates has generated seismicity

566   since the late Miocene, the Exmouth Plateau is considered a tectonically quiescent passive-

567   margin setting, characterised by low seismicity and the absence of major deformation processes

568   (Albini et al., 2013; Nugraha et al., 2018). The seismicity of an area can alter the initial (i.e.,

569   immediately post-depositional) sediment properties. For example, siliciclastic sediments

570   within the first 100 m below the seabed that are exposed to repetitive low-magnitude

571   earthquakes can progressively increase their shear strength through shear-induced compaction

572   and dewatering (a process termed seismic strengthening; Sawyer and DeVore, 2015; Ten Brink

573   et al., 2016). Therefore, siliciclastic sediments on active margins typically have higher

574   undrained shear strength and can withstand higher static and dynamic shear stresses than

575   sediments at equivalent depths on relatively aseismic passive margins (Figure 18B; Nelson et

576   al., 2011; Sawyer and DeVore, 2015; Ten Brink et al., 2016). Conversely, when repetitive

577   seismicity (thus the seismic strengthening process) is absent, sediments have lower shear

578   strengths (Figure 18B) and are more susceptible to slope failures than those on active margins

579   (i.e. Sawyer and DeVore, 2015; DeVore and Sawyer, 2016). The shear strength of the carbonate

580   ooze in the Kangaroo Syncline ranges from 1.2 kPa to 12.5 kPa in shallow (i.e., <100 meters

581   below seabed) sediments (Figure 18B), which is at the lower end of the passive margin trend

582   and does not show any evidence for seismic strengthening (i.e., the undrained shear strength is

583   markedly lower than values characterising active margins). Carbonate oozes in Kangaroo

584   Syncline may thus be extremely unstable due to their extremely low shear strength that in part

585   is linked to the low seismicity of the margin.

5.1.4 Slope Steepening Driven by Tectonic Uplift and Sedimentation

During the mid to late Miocene, the northward collision of the Australian Plate with Eurasian microplates induced compressional deformation offshore NW Australia, resulting in broad folding of the seabed and the formation of the Exmouth Plateau Arch (Boyd et al., 1993). This tectonic uplift increased the seabed gradient between the plateau arch and the adjacent continental slope (Figure 1C). Since the late Miocene, the region has experienced widespread MTC emplacement, with sediment sourced from the uplifted plateau arch and adjacent slope (Hengesh et al., 2013; Scarselli et al., 2013b). Published studies attribute the development of widespread MTCs sourced from the uplifted plateau arch and adjacent slope to tectonically induced tilting and folding of the seabed, which enhanced slope gradients and promoted gravity-driven sediment failures (Nugraha et al., 2018).

Similar features have been observed in the Qiongdongnan (QDN) Basin, northern South China Sea, where recurrent slope failures have occurred since the late Miocene, leading to the accumulation of stacked MTCs. During the late Miocene, tectonic uplift of the Himalaya–Tibetan Plateau intensified erosion and weathering in its catchment areas, substantially increasing the sediment supply transported by the paleo-Red River into the QDN Basin (Zhao et al., 2019; Li et al., 2022). In response to this increased sediment flux, the continental margin began to prograde, constructing large-scale clinothems with steep foresets that advanced basinward (Chen et al., 2020). These stacked clinothems led to slope oversteepening and widespread instability, culminating in the development of extensive MTCs throughout the Pliocene succession. A comparable process has been documented in the Taranaki Basin (New Zealand), where tectonic uplift enhanced sedimentation rates and drove the formation of extensive clinoform systems, steepening the paleo-seafloor gradient and preconditioning the margin for repeated slope failure (Sharman et al., 2015; Franzel and Back, 2019).

610 In summary, the high abundance of MTCs in the Kangaroo Syncline reflects the combined

611 influence of persistent carbonate ooze deposition, excess pore pressure associated with vertical

612 fluid migration, broad-scale tectonic uplift during the mid-late Miocene, although not

613 associated with strong deformation or seismicity, nevertheless contributed to progressive slope

614 steepening, and low sediment shear strength due to the absence of seismic strengthening.

5.2 How do preexisting MTCs influence later slope failures?

616 We identify five ways that preexisting MTCs can influence the emplacement of subsequent

617 slope failures.

5.2.1. Buried MTCs and their Role in Slope Failure Preconditioning

619 An overriding MTC can drive density increases and permeability decreases in the substrate,

620 resulting in shear compaction (Wu et al., 2021a). The basal shear surfaces of MTCs are

621 generally more consolidated than lithologically comparable slope or basin-floor strata, showing

622 high bulk density and shear strength, low porosity and permeability. Basal shear surfaces may

623 therefore represent intra-stratal hydraulic boundaries, influencing or limiting fluid migration

624 and the related distribution of overpressure, and thus the overall strength profile of the

625 sedimentary succession (Wu et al., 2021a).

626 In the Kangaroo Syncline, prior to the emplacement of MTC-2, the basal shear surface of MTC-

627 1 may have formed a hydraulic boundary within the carbonate ooze-dominated succession

628 (Figure 3C). This hydraulic boundary may have permitted the build-up of excess pore pressure

629 and generation of weak layers within the substrate, ultimately priming slope failure and the

630 formation and emplacement of MTC-2.

5.2.2. Relief-Induced Partitioning as a Kinematic Control on Subsequent Slope Failures

632   MTC emplacement can remould the seascape, creating giant, scarp-bound seabed depressions

633   that cover thousands of square kilometres, and that change the slope profile, potentially making

634   future failures more likely (i.e. Kneller et al., 2016). Previous studies suggest that relief above

635   MTCs influence pathways of subsequent sediment gravity flows. However, the way in which

636   preexisting MTCs control the flow direction, depositional pattern, and stratigraphic

637   architecture of subsequent failures has received less attention.

638   In the Kangaroo Syncline, we show that the large blocks (c. 300 m thick) within MTC-2 formed

639   substantial relief (i.e., >100 m and that extends 10's of km laterally) on the contemporaneous

640   seabed (Figure 4D). This relief controlled the down-dip extent and style of strain within MTC-

641   3, with shortening and thrusting occurring where it impinges on this relief (bathymetrical

642   control; Figures 5E). Whereas MTC-3 largely healed the accommodation created by failure of

643   slope material comprising MTC-2, some accommodation remained between blocks within

644   MTC-2. For example, the remaining accommodation above MTC-3 contributed to the

645   partitioning of MTC-8 (Figure 9A, 9D). Slope breaks formed by relief along MTC-2 are

646   expressed within the basal shear surface of MTC-8, evident as the relief of MTC-8's basal shear

647   surface is lower immediately adjacent to the headwall scarp of MTC-2, accompanied by

648   directional changes in striation patterns and thus emplacement direction, and increases in both

649   the incision depth and width of basal grooves (Figures 11A-C). This indicates the former

650   controlled the emplacement direction and erosional capacity of the latter. Relief associated with

651   preexisting MTCs can therefore serve as structural weak zones (i.e., deformational foci) that

652   localize deformation, influence the emplacement, distribution, and erosional capacity of

653   subsequent MTCs. This is consistent with the findings of Safadi et al. (2017), who demonstrate

654   that large-scale buried MTCs can form a seabed low, acting as long-lived deformational foci

655   that influence the subsequent MTCs over a few hundred thousands of years. Since the main

656   energy of the tsunami waves travel in the direction of slope failure motion, the failure direction

657 is as important as the speed and scale of movement (Driscoll et al., 2000; Schnyder et al., 2016).

658 We suggest that conducting subsurface and surface mapping of MTC top surfaces, particularly

659 at locations where large blocks and scarps exist, could help in predict future slope failure routes

660 and potential danger zones (i.e., pathways for subsequent failure processes), thereby reducing

661 geohazard risks to seabed infrastructure.

662 *5.2.3. Basal Shear Surfaces as Erosional Limits to Recurrent Slope Failures*

663 Commonly, the basal shear surface of MTCs is expressed as a high-amplitude, continuous

664 seismic reflection with reversed polarity relative to the seabed, representing the densest part of

665 the deposit. Such surfaces may also serve as a key kinematic boundary, along which slope

666 failure occurs and MTCs are translated (Shipp, 2004; Sawyer, 2007; Wu et al., 2021a). In the

667 Kangaroo Syncline, MTC-6 has an extensive basal shear surface with a minimum mapped area

668 of ~1,800 km² (Figures 8A, 8B). Subsequent MTCs (MTC-7 to MTC-9) share this basal shear

669 surface near the headwall region, indicating a composite kinematic boundary for recurrent

670 slope failure (Figure 8E). The shared basal shear surface of the stacked MTCs in the Kangaroo

671 Syncline suggests that the basal shear surface of the buried MTCs, particularly MTC-6, acted

672 as a structural detachment for subsequent mass-transport events. Although later MTCs may

673 erode or deform the underlying deposits, the initial basal shear surface likely represents a

674 mechanically strong and compacted boundary that resists further incision. This mechanical

675 boundary may limit the depth of subsequent failure surface propagation, thereby constraining

676 the volume of sediment that can be entrained and transported during subsequent slope failures.

677 *5.2.4. Long-Term Seabed Shaping by Differential Compaction Over Buried MTCs*

678 Differential compaction is intrinsic to MTC emplacement, driven by rheological contrasts

679 between rapidly compacting ductile debris flows and less-deformed transport or remnant

680 blocks (Alves, 2010). This results in downward bending of strata over debritic material and

681 upward bending over blocks, producing rugose MTC top surfaces with notable relief (e.g.,

682 Alves and Cartwright, 2010). Such compaction can persist for millions of years, shaping seabed

683 morphology and influencing slope depositional patterns (e.g., Alves, 2010; Ward et al., 2018).

684 In the Kangaroo Syncline, differential compaction between megaclasts or transported blocks

685 and the surrounding debritic matrix has produced significant topographic relief, ranging from

686 tens to over a hundred meters in height and hundreds of meters in width (Figures 14C, 14D,

687 15B, 15C). These protruding megaclasts, termed "shield blocks" (Rusconi, 2017), can act as

688 physical barriers that obstruct, deflect, or modify the dynamics of succeeding slope failures.

689 For example, the top surface of MTC-9 preserves distinct bathymetric highs, indicating that

690 these irregularities remained exposed and were not buried during the deposition of MTC-9

691 (Figures 15B, 15C). When subsequent slope failures encounter these obstacles, the flow is

692 forced to diverge around them, potentially generating localised downslope turbulence with

693 enhanced erosive capacity against the substrate. This is evidenced by the basal shear surface

694 (BSS) of the subsequent MTC, which exhibits a steep gradient and increased thickness on the

695 lee side, and a reduced thickness on the gentle stoss side above the buried blocks, indicating

696 that debris flows had enhanced erosive capacity in these zones (e.g., Figure 15B). This

697 turbulence persists some distance, until the younger MTC is physically impeded by the

698 underlying blocks. This mechanism is analogous to the transition from a normal to a

699 supercritical turbidity current, in which flow rheology is highly influenced by preexisting

700 bathymetric highs (e.g., Covault et al., 2017; Fildani et al., 2021).

701 In the case of MTC-11, the deposit exhibits a hybrid frontal morphology, i.e., it is frontally

702 confined in its central portion, where blocks within the underlying MTC-9 act as topographic

703 barriers, whereas its lobate margins are frontally emergent, reflecting the absence of such

704 obstacles (Figures 16C, 16D). This spatial variability underscores the critical role of inherited

705 relief, generated by differential compaction, in modulating the rheology of the overriding flow

706 and potentially enhancing the run-out distance of the subsequent MTC (e.g., Moernaut and De

707 Batist, 2011; Nugraha et al., 2020). Therefore, block-induced differential compaction within

708 buried MTCs can generate basal topographic obstacles that exert a first-order control on the

709 frontal style and kinematic behaviour of ensuing mass movements, ultimately influencing their

710 downslope translation and run-out distance.

711 *5.2.5. Mapping Buried MTCs to Predict Future Slope Failure Depocenters*

712 Slope failure is often associated with the formation of large evacuation zones and steep

713 headwall scarps (e.g., Solheim et al., 2005; Nugraha et al., 2022). In the Kangaroo Syncline,

714 the initiation of MTC-2 created a large evacuation zone characterised by >200 m of vertical

715 relief and a c. 30 km long, NNE-SSW oriented headwall scarp (Figure 4A). This headwall

716 scarp separated the paleo-seabed into bathymetrically high and low areas in the east and west,

717 respectively. This feature subsequently influenced the relief associated with the basal shear

718 surface of younger MTCs. For example, the basal shear surfaces of subsequent MTC-8 and

719 MTC-9 dip relatively steeply near MTC-2's headwall scarp (Figures 9A, 13A). The headwall

720 scarp associated with MTC-2 also influenced the thickness distribution of subsequent MTCs.

721 For example, MTC-8 is thicker in the low area immediately adjacent to the headwall scarp of

722 MTC-2 (Figure 13). The headwall scarp of preexisting MTC-2 may therefore control seabed

723 relief and local thickness changes in younger MTCs for a relatively long time after initial

724 formation.

725 In the Kangaroo Syncline, the spatial distribution of younger MTCs is often controlled by local

726 topographic highs generated above preexisting MTCs, with their boundaries coinciding with

727 areas where preexisting MTCs are locally thickest (i.e., MTC-2 vs MTC-3; MTC-9 vs MTC-

728 10; Figure 17). We show that in areas where preexisting MTCs are relatively thick, subsequent

729 MTCs are relatively thin, and vice versa. For example, the deposition of MTC-9 exhibits a

730   thick-thin-thick pattern (Figure 13C), and the younger MTC-10 is confined to areas where the

731   underlying MTC-9 is relatively thin (Figure 16B); a similar thickness inter-relationship occurs

732   in younger stratigraphy, with MTC-11 being restricted to areas where the underlying MTC-9

733   is relatively thin (Figure 16D). We note the emplacement of a younger MTC may erode

734   preexisting MTCs, modifying their original thickness distribution. However, because gravity-

735   driven slope failures are sensitive to variations in slope gradient, they are preferentially

736   accommodated in bathymetrically low regions (Kneller et al., 2016). We therefore suggest that

737   the buried MTCs can exert a primary control on the thickness distribution of subsequent slope

738   failures. Detailed mapping of MTCs is therefore essential in slope failure-prone areas, noting

739   that future subsea construction should avoid areas where seabed MTCs are relatively thin,

740   given this may represent the depocentre for a future MTC (Figure 17).

741   ## 5.3 Limitations and Suggestions for Future Work

742   Although the proposed priming mechanisms for recurrent slope failures in the Kangaroo

743   Syncline are consistent with the available geological and geophysical evidence, several aspects

744   of our interpretation remain constrained by data availability. Firstly, although well data

745   constrain the broader stratigraphy and the position of key seismic reflections (e.g., the late

746   Miocene unconformity), dating of individual MTCs is not possible with the existing data. This

747   chronostratigraphic limitation, which is common to most subsurface investigations studies due

748   to the high cost and technical difficulty of deep-sea drilling, precludes quantification of slope

749   failure recurrence intervals. Future work incorporating biostratigraphic or radiometric age

750   determinations from targeted cores would improve the temporal framework and enable detailed

751   assessment of failure frequency and the longevity of inherited bathymetry.

752   Secondly, the interpretations of sediment properties and vertical fluid migration rely on ODP

753   data, regional analogues, and seismic attributes analyses. Although fluid migration is widely

754 documented across the Exmouth Plateau, direct measurements such as CPTu profiles, vane-

755 shear tests, pore-pressure records, or amplitude-versus-offset analyses are not available within

756 the cube. Obtaining such high-quality in-situ measurements in future drilling campaigns, or in

757 other MTC-rich passive margins, would provide better constraints on failure mechanisms,

758 pore-pressure evolution, and sediment rheology before and after failure.

759 Finally, several MTCs extend beyond the boundaries of the 3D seismic reflection cube,

760 resulting in incomplete imaging of their distal, lateral margins or headwall regions (e.g.,

761 western parts of MTC-3). Where margins are open, the true extent of deposits, potential off-

762 cube thickening, or alternative routing pathways cannot be fully resolved. As such,

763 interpretations of transport directions, lateral confinement, and depocentre in these areas should

764 be considered with appropriate caution. Expanded seismic coverage or integration with

765 adjacent datasets would help refine these interpretations in the future. Together, these

766 limitations highlight the value of future integrated studies that combine new ocean scientific

767 drilling, geotechnical testing, and broader seismic coverage to further validate the mechanisms

768 proposed here and improve geohazard assessments on passive margins.

6. Conclusions

770 Our study provides a valuable case study on the dynamic interactions and influence between

771 eleven stacked MTCs and enables a better understanding of slope failure mechanisms in

772 passive margins globally. Based on the results of this study, the following conclusions can be

773 drawn:

774 (1) We reveal that the Kangaroo Syncline accommodate at least eleven large stacked MTCs

775   that comprise nearly 80% of the total stratigraphy. We suggest that the Kangaroo Syncline

776   is particularly prone to slope failure because of the interplay of four factors: widespread

777   and sustained carbonate ooze deposition, the abundance of vertical fluid migration, the lack

778   of seismic strengthening process, and tectonically induced increases in seabed gradient.

779   (2) We demonstrate that preexisting MTCs can have far-reaching effects on the stability of the

780   surrounding sediment pile. Potentially, MTC emplacement can trigger differential

781   compaction and headwall scarp effect that influences the bathymetry, distribution and

782   emplacement of subsequent slope failures. More specifically, preexisting MTCs can affect

783   lithology composition, provide bathymetric constraints to failure displacement, redirect

784   flow pathways, control runout distances and enhance the erosion capacity of the subsequent

785   slope failures.

786   (3) Our results demonstrate that buried MTCs exert a significant influence on subsequent slope

787   failure distribution patterns and their depocentre. Therefore, measuring the preexisting

788   MTCs (especially their top surface) provides a unique analogue for predicting future MTC

789   locations and providing key information for the planning of future seabed infrastructure

790   and hazards mitigation.

Table Caption

792   Table 1. Summary of the source areas, transport directions, kinematic indicators, thickness

793   patterns, and inferred influence on subsequent events for all mapped mass transport complexes

794   (MTCs) in the study area.

Figure Caption

796   Figure 1. (A) The bathymetric map of the NW Australian region shows the study area location,

797   key tectonic structures, and location of datasets. The location of ODP 762 is marked as a red

798   dot, the Willem 3D seismic is indicated by a red polygon and the 2D seismic data by a solid

799   grey line. (B) Tectonostratigraphic chart for the study area, lithology and age is defined in the

800   ODP 762 report. All data relating to the ODP log is depth below the seabed from ODP site 762.

801   (C) Regional seismic section through the Exmouth Plateau Arch, Kangaroo Syncline and the

802   lower continental slope. Horizon H0 is the base of the study interval and has been tied to the

803   late Miocene Unconformity surface. H0 is equivalent to Reflector 7 of Boyd et al. (1993), N17–

804   1 horizon of Hull and Griffiths (2002), Horizon C of Nugraha et al. (2018), and Horizon H2 of

805   Wu et al. (2023). See Figure 1A for the location of Figure 1C.

806   Figure 2. (A) The regional seismic section through the Willem 3D shows the study interval and

807   the late Miocene Unconformity surface (H0). (B) Sketches showing the location of stacked

808   MTCs 1-6, undifferentiated MTCs and key seismic horizons (H1-seabed). (C) Zoomed-in view

809   of the Willem 3D survey area, showing the locations of Figures 3, 4, and 5 presented in this

810   study. (D) Zoomed-in view of the Willem 3D survey area, showing the locations of Figures 6

811   and 7 presented in this study. The location of Figures 2C and 2D is indicated in Figure 2A.

812   Figure 3. (A) Variance attribute map calculated on the basal shear surface (H1) of MTC-1,

813   showing the boundaries and internal key structures of the MTC-1. (B) Interpreted sketch of

814   MTC-1, showing the boundaries and internal key structures of the MTC-1. (C) The seismic

815   section cutting through MTC-1 and MTC-2 shows the detailed structures and seismic

816   characters. (D) The seismic section cutting along the transport direction of MTC-1. See Figure

817   3B for location.

818   Figure 4. (A) Uninterpreted variance attribute map calculated on the basal shear surface (H3)

819   of MTC-2, showing the boundaries and internal key structures of the MTC-2. (B) Interpreted

820   sketch of MTC-2, showing the MTC boundaries, key kinematic indicators and the transport

821   direction. (C) Isochron (TWT thickness) map of MTC-2, indicating a westward thickness

822   thinning trend. The contour interval is 60 ms. (D) The seismic section cutting through MTC-2

823 and MTC-3 shows the detailed structures and seismic characters. See the location of this

824 seismic section in Figure 4B.

825 Figure 5. (A) Uninterpreted variance attribute map calculated on the basal shear surface (H5)

826 of MTC-3, showing the boundaries and internal key structures of the MTC-3. (B) Interpreted

827 sketch of MTC-3, showing its boundaries and key kinematic indicators. (C) Isochron (TWT

828 thickness) map of MTC-3, indicating an eastward thickness thinning trend. The contour

829 interval is 60 ms. (D) The seismic section cuts through the scours of MTC-3, showing the cross-

830 sectional profile of the scours. (E) The seismic section cuts through the eastern margin of MTC-

831 3, showing the thrust terminating against the underlying spread blocks. See the location of the

832 seismic sections in Figure 5B.

833 Figure 6. (A) Variance attribute map calculated on the basal shear surface (H7) of MTC-4,

834 showing the boundaries and internal key structures of the MTC-4. (B) Spectral decomposition

835 calculated from the basal shear surface of MTC-4, providing a detailed view of the internal

836 fingerprint-like structures and boundaries of this MTC. (C) Interpreted sketch of MTC-4,

837 illustrating external geometry and key kinematic indicators. (D) The seismic section cutting

838 through MTC-4 shows its detailed structure and internal seismic characteristics. The white

839 dashed line marks a flattened surface to better visualize MTC-4, and the white arrow indicates

840 its transport direction. The location of this seismic section is shown in Figure 4C.

841 Figure 7. (A) Variance attribute map calculated on the basal shear surface (H9) of MTC-5,

842 showing the boundaries and internal key structures. (B) Spectral decomposition calculated

843 from the basal shear surface of MTC-5, showing detailed fingerprint-like internal structures

844 and boundaries. (C) Interpreted sketch of MTC-5, showing the external geometry and internal

845 structural details. (D) The seismic section cutting through MTC-5 shows its detailed structure

846 and internal seismic characteristics. The white dashed line marks a flattened surface to better

847 visualize MTC-5, and the white arrow indicates its transport direction. The location of this

848 seismic section is shown in Figure 5C.

849 Figure 8. (A) Variance attribute map calculated on the basal shear surface (H11) of MTC-6,

850 showing the boundaries and internal key structures. (B) Interpreted sketch of MTC-6, showing

851 the external geometry and internal structural details. (C) Variance attribute map calculated on

852 the basal shear surface (H13) of MTC-7, showing the boundaries and internal key structures.

853 (D) Interpreted sketch of MTC-7, showing the external geometry and internal structural details.

854 Figure 9. (A) Bathymetric map calculated on the basal shear surface (H15) of MTC-8, showing

855 the paleoseafloor bathymetry. (B) The uninterpreted variance attribute map calculated on the

856 basal shear surface of MTC-8 shows the MTC's boundaries and internal key structures. (C)

857 Interpreted sketch of MTC-8, showing the MTCs boundaries and key kinematic indicators. (D)

858 Isochron (TWT thickness) map of MTC-8, the contours are every 60 ms. (E) Seismic section

859 cutting through MTC-8 shows the relief variation near the headwall scarp of MTC-2 and

860 groove details. See the location of the seismic section in Figure 9C.

861 Figure 10. (A) Seismic section cutting across the grooves of MTC-8, with the basal shear

862 surface shown in 3D view. The location of this seismic section is shown in Figure 9C. (B)

863 Zoom-in view of the protruding structure developed on the basal shear surface of MTC-8, this

864 attribute is attracted 15 ms above the basal shear surface. See location in Figure 9C. (C) Seismic

865 section cut along the dip of the protruding structure, showing the internal seismic facies.

866 Figure 11. (A) Zoom-in map of Figure 9A, showing directional changes of grooves on the basal

867 shear surface of MTC-8 near a NW-trending lineation. Note the NW-trending lineation

868 corresponds with the headwall scarp of MTD-2, lying below. The location of Figure 11A is

869 shown in Figure 9C. (B) Zoom-in view illustrate the width and incision depth of G-1 in cross-

870 section. Groove width was measured between opposing flanks, while incision depth was taken

871 from the groove base to the reference level defined by the undeformed basal shear surface. (C)

872 Zoom-in view and the cross-sectional geometry at the groove termination. (D) The Rose

873 diagram shows the orientation of the grooves, blue indicates grooves developed outside the

874 NW-trending lineation, and red indicates grooves developed within the NW-trending lineation.

875 (E) The width and incision depth of groove G-1, see the location of groove G-1 in Figure 11A.

876 Figure 12. 3D view of MTC-8's basal shear surface, showing a well-developed field of grooves.

877 The extent of this figure is the same as in Figure 11A, but the viewing angle is rotated 180°

878 counterclockwise.

879 Figure 13. (A) Uninterpreted variance attribute map calculated on the basal shear surface (H17)

880 of MTC-9, showing the boundaries and internal key structures of the MTC-9. (B) Interpreted

881 sketch of MTC-9, showing the boundaries, headwall scarp, internal blocks and other kinematic

882 indicators of this MTC. (C) Isochron (TWT thickness) map of MTC-9, revealing a thick-thin-

883 thick tripartite pattern. (D) Bathymetric map calculated on the top surface (H18) of MTC-9,

884 showing the block associated paleoseabed bathymetry.

885 Figure 14. (A) Zoomed-in view of the basal shear surface of MTC-9, showing NNW-trending

886 scours. The location of Figure 14A is indicated in Figure 13A. (B) Zoomed-in view of the top

887 surface of MTC-9, showing the tips of intruding blocks on the paleoseabed. The location of

888 Figure 14B is indicated in Figure 13D. (C) Seismic dip section along the scours, showing the

889 internal seismic facies of megaclasts and the rugged top surface of MTC-9. (D) Seismic cross

890 section along the scours, showing the internal seismic facies of megaclasts and the rugged top

891 surface of MTC-9. See the locations of seismic section in Figure 14A.

892 Figure 15. (A) Zoomed-in view of the basal shear surface of MTC-9, showing transported

893 blocks near the headwall scarp. The location of Figure 15A is indicated in Figure 13A. (B) The

894 seismic section crosses the area of the headwall scarp and translated blocks of the MTC-9. Note

895   the basal shear surface's step-shaped geometry near the headwall and the rugged top surfaces.

896   (C) Seismic section across transported blocks, showing their internal seismic characteristics

897   and rugged top surfaces. The locations of Figures 15B and 15C are indicated in Figure 15A.

898   (D) Seismic section cutting across the remnant block, showing its boundary and internal

899   seismic facies. The location of this seismic section is shown in Figure 13B.

900   Figure 16. (A) The variance attribute map calculated on the basal shear surface (H19) of MTC-

901   10 shows the MTC's boundaries and internal key structures. (B) Isochron (TWT thickness) map

902   of MTC-10, showing the depocentre of the MTC-10. (C) The variance attribute map calculated

903   on the basal shear surface (H21) of MTC-11 shows the MTC's boundaries and internal key

904   structures. (B) Isochron (TWT thickness) map of MTC-11, showing the depocentre of the

905   MTC-11.

906   Figure 17. (A) Seismic cross section cutting across the MTC-10 and MTC-11, showing the

907   thickness of these MTCs pinch-out at the local topography high created by the underlying

908   MTC-9. See the location in Figure 16A. (B) Seismic dip section cutting across the central

909   frontally confined domain of MTC-11, showing that MTC-11 terminates against blocks within

910   the underlying MTC-9. (C) Seismic dip section cutting across the frontally emergent domain

911   of MTC-11, showing that MTC-11 was able to transport downslope without obstruction where

912   underlying blocks are absent in MTC-9. The locations of Figures 17B and 17C are indicated in

913   Figure 16C.

914   Figure 18. The composite diagram of the MTCs thickness relationships, notes that the Y axis

915   stands for thickness in time, and the X axis indicates the length in kilometres. Generally,

916   younger MTCs thicken in areas where older MTCs are relatively thinner, and vice versa.

917   Figure 19. (A) Shear strength degradation of carbonate oozes during cyclic T-bar penetrometer

918   tests, modified from Gaudin and White (2009). The loss of strength is expressed as the ratio of

the remoulded shear strength to the intact shear strength, experienced by different soils during cycles of remoulding for siliciclastic sediments and carbonate oozes of the offshore NW Australia. (B) Undrained shear strength measurements from the Ocean Drilling Program and Integrated Ocean Drilling Program. Nine type sites are chosen from the top 100 m below seabed sediment and are normally consolidated on active and passive margins. Active margin sites include offshore Japan (Site C0001), Cascadia (Site U1329), and two sites offshore Costa Rica (Sites 1039 and U1414). Passive margin sites include Amazon Fan (Site 942), Madeira abyssal plain (Site 951), New Jersey (Site 1073), Carolina Slope (Site 1054), and Exmouth Plateau and Kangaroo Syncline (ODP 762). The shear strength of the carbonate ooze in the Kangaroo Syncline is lower than that of siliciclastic sediments on other passive margins, and that is significantly lower than that of siliciclastic sediments on active margins. Data sets for this figure are adopted from the global survey of Sawyer and DeVore (2015). Black and red lines are the average undrained shear strength for passive and active margins, respectively.

948 Table 1. Summary of the source areas, transport directions, kinematic indicators, thickness patterns, and inferred influence on subsequent events for all
949 mapped mass transport complexes (MTCs) in the study area

MTC	Source area	Transport direction	Kinematic indicators	Thickness pattern	Influence on subsequent MTCs
MTC-1	Kangaroo Syncline	WNW	Grooves, pressure ridges, frontal ramp	-	Forms intra-stratal hydraulic boundaries that precondition MTC-2
MTC-2	Continental slope	WNW	Grooves, internal ramps, contractional thrusts	Thick in SW, thinning to NE	Creates substantial inherited relief; thicker areas deflect MTC-3 and inhibit runout
MTC-3	Exmouth Plateau	WSW	Grooves, fold-thrust pairs	Thick toward NE, thinning to SW	-
MTC-4	Kangaroo Syncline	NNW	Popup blocks, thrusts, internal ramps	Thickest above thin areas of underlying MTC-3	-
MTC-5	Continental slope	NW	Popup blocks, thrusts, lateral margins	Thick in NE, thinning basinward	-
MTC-6	Continental slope	NNW	Continuous internal ramp, grooves	Thick in central zone, thinning upslope	Produces regional basal shear surface that acts as erosional limits to subsequent MTCs
MTC-7	Continental slope	NNW	Grooves, internal ramp, headwall scarp	Thick above thin portions of underlying MTC-6	Steers MTC-8 around giant blocks and enhances downslope divergence
MTC-8	Continental slope	NW	Internal ramp, mega clasts, groove field	Thickened where BSS cuts deeper stratigraphy	Creates topographic highs that strongly affect MTC-9 pathway
MTC-9	Continental slope	NW	Transported blocks, remnant blocks, scours	Thick-thin-thick tripartite thickness distribution pattern	Long-term differential compaction creates seabed irregularities that control distribution and thickness pattern of subsequent MTCs
MTC-10	Continental slope	NW	Lateral margins, grooves	Deposits only where underlying MTC-9 is thin	Spatially restricted by MTC-9 thick zones; beginning of frontally confined or emergent transition
MTC-11	Continental slope	NW	Two distinct frontal morphologies (confined vs emergent), grooves	Deposits only where underlying MTC-9 is thin	Flow partitioning caused by underlying MTC-9

950

References

Abu, C., Jackson, C. A.-L., and Francis, M., 2022, Strike-slip overprinting of initial co-axial shortening within the toe region of a submarine landslide and a model for basal shear surface growth: a case study from the Angoche Basin, offshore Mozambique: Journal of the Geological Society, v. 179, no. 2.

Albini, P., Musson, R., Gomez Capera, A., Locati, M., Rovida, A., Stucchi, M., and Viganò, D., 2013, Global historical earthquake archive and catalogue (1000-1903): Pavia, Italy.

Alves, T. M., 2010, 3D Seismic examples of differential compaction in mass-transport deposits and their effect on post-failure strata: Marine Geology, v. 271, no. 3-4, p. 212-224.

Alves, T. M., and Cartwright, J. A., 2010, The effect of mass-transport deposits on the younger slope morphology, offshore Brazil: Marine and Petroleum Geology, v. 27, no. 9, p. 2027-2036.

Aqrawi, A. A., and Bø, T. H., 2016, Amplitude contrast seismic attribute, Google Patents.

Barber, P., 1988, The Exmouth Plateau deep water frontier: a case history.

Barrett, R., Bellwald, B., Talling, P., Micallef, A., Gross, F., Berndt, C., Planke, S., Myklebust, R., and Krastel, S., 2021, Does retrogression always account for the large volume of submarine megaslides? Evidence to the contrary from the Tampen Slide, offshore Norway: Journal of Geophysical Research: Solid Earth, v. 126, no. 2, p. e2020JB020655.

Bellwald, B., Manton, B., Lebedeva-Ivanova, N., Zastrozhnov, D., Myklebust, R., Planke, S., Forsberg, C. F., Vanneste, M., and Locat, J., 2024, Rapid glacial sedimentation and overpressure in oozes causing large craters on the mid-Norwegian margin: integrated interpretation of the Naust, Kai and Brygge formations.

Berndt, C., Costa, S., Canals, M., Camerlenghi, A., de Mol, B., and Saunders, M., 2012, Repeated slope failure linked to fluid migration: the Ana submarine landslide complex, Eivissa Channel, Western Mediterranean Sea: Earth and Planetary Science Letters, v. 319, p. 65-74.

Boyd, R., Williamson, P., and Haq, B., 1993, Seismic Stratigraphy and Passive‐Margin Evolution of the Southern Exmouth Plateau: Sequence Stratigraphy and Facies Associations, p. 579-603.

Bryn, P., Berg, K., Forsberg, C. F., Solheim, A., and Kvalstad, T. J., 2005, Explaining the Storegga slide: Marine and Petroleum Geology, v. 22, no. 1, p. 11-19.

Bull, S., Cartwright, J., and Huuse, M., 2009, A review of kinematic indicators from mass-transport complexes using 3D seismic data: Marine and Petroleum Geology, v. 26, no. 7, p. 1132-1151.

Bünz, S., Mienert, J., Bryn, P., and Berg, K., 2005, Fluid flow impact on slope failure from 3D seismic data: a case study in the Storegga Slide: Basin Research, v. 17, no. 1, p. 109-122.

Cathro, D. L., and Karner, G. D., 2006, Cretaceous–Tertiary inversion history of the Dampier Sub-Basin, Northwest Australia: insights from quantitative basin modelling: Marine and Petroleum Geology, v. 23, no. 4, p. 503-526.

Chen, S., Steel, R., Wang, H., Zhao, R., and Olariu, C., 2020, Clinoform growth and sediment flux into late Cenozoic Qiongdongnan shelf margin, South China Sea: Basin Research, v. 32, no. Clinoforms and Clinothems: Fundamental Elements of Basin Infill, p. 302-319.

Covault, J. A., Kostic, S., Paull, C. K., Sylvester, Z., and Fildani, A., 2017, Cyclic steps and related supercritical bedforms: building blocks of deep-water depositional systems, western North America: Marine Geology, v. 393, p. 4-20.

Davies, R. J., and Clark, I. R., 2006, Submarine slope failure primed and triggered by silica and its diagenesis: Basin Research, v. 18, no. 3, p. 339-350.

DeVore, J. R., and Sawyer, D. E., 2016, Shear strength of siliciclastic sediments from passive and active margins (0–100 m below seafloor): insights into seismic strengthening, Submarine Mass Movements and their Consequences, Springer, p. 173-180.

Dott Jr, R., 1963, Dynamics of subaqueous gravity depositional processes: AAPG Bulletin, v. 47, no. 1, p. 104-128.

999   Driscoll, N. W., Weissel, J. K., and Goff, J. A., 2000, Potential for large-scale submarine slope failure
1000   and tsunami generation along the US mid-Atlantic coast: Geology, v. 28, no. 5, p. 407-410.
1001   Exon, N., Haq, B., and Von Rad, U., Exmouth Plateau revisited: scientific drilling and geological
1002   framework, *in* Proceedings Proceedings of the Ocean Drilling Program, Scientific
1003   Results1992, Volume 122, Ocean Drilling Program College Station, Tex, p. 3-20.
1004   Fildani, A., Kostic, S., Covault, J. A., Maier, K. L., Caress, D. W., and Paull, C. K., 2021, Exploring a new
1005   breadth of cyclic steps on distal submarine fans: Sedimentology, v. 68, no. 4, p. 1378-1399.
1006   Franzel, M., and Back, S., 2019, Three-dimensional seismic sedimentology and stratigraphic
1007   architecture of prograding clinoforms, central Taranaki Basin, New Zealand: International
1008   Journal of Earth Sciences, v. 108, no. 2, p. 475-496.
1009   Frey-Martínez, J., Cartwright, J., and James, D., 2006, Frontally confined versus frontally emergent
1010   submarine landslides: a 3D seismic characterisation: Marine and Petroleum Geology, v. 23,
1011   no. 5, p. 585-604.
1012   Frey Martinez, J., Cartwright, J., and Hall, B., 2005, 3D seismic interpretation of slump complexes:
1013   examples from the continental margin of Israel: Basin Research, v. 17, no. 1, p. 83-108.
1014   Gatter, R., Clare, M., Kuhlmann, J., and Huhn, K., 2021, Characterisation of weak layers, physical
1015   controls on their global distribution and their role in submarine landslide formation: Earth-
1016   Science Reviews, v. 223, p. 103845.
1017   Gaudin, C., and White, D., 2009, New centrifuge modelling techniques for investigating seabed
1018   pipeline behaviour.
1019   Gavey, R., Carter, L., Liu, J. T., Talling, P. J., Hsu, R., Pope, E., and Evans, G., 2017, Frequent sediment
1020   density flows during 2006 to 2015, triggered by competing seismic and weather events:
1021   Observations from subsea cable breaks off southern Taiwan: Marine Geology, v. 384, p. 147-
1022   158.
1023   Gee, M., Gawthorpe, R., and Friedmann, J., 2005, Giant striations at the base of a submarine
1024   landslide: Marine Geology, v. 214, no. 1-3, p. 287-294.
1025   Haq, B. U., Boyd, R. L., Exon, N. F., and von Rad, U., 1992, 47. EVOLUTION OF THE CENTRAL
1026   EXMOUTH PLATEAU: A POST-DRILLING PERSPECTIVE1.
1027   Harbitz, C. B., Løvholt, F., and Bungum, H., 2014, Submarine landslide tsunamis: how extreme and
1028   how likely?: Natural Hazards, v. 72, no. 3, p. 1341-1374.
1029   Hengesh, J., Dirstein, J., and Stanley, A., 2013, Landslide geomorphology along the Exmouth plateau
1030   continental margin, North West Shelf, Australia: Australian Geomechanics Journal, v. 48, no.
1031   4, p. 71-92.
1032   Hengesh, J., Dirstein, J. K., and Stanley, A. J., 2012, Seafloor geomorphology and submarine landslide
1033   hazards along the continental slope in the Carnarvon Basin, Exmouth Plateau, North West
1034   Shelf, Australia: The APPEA Journal, v. 52, no. 1, p. 493-512.
1035   Hodgson, D., Brooks, H., Ortiz-Karpf, A., Spychala, Y., Lee, D., and Jackson, C.-L., 2018, Entrainment
1036   and abrasion of megaclasts during submarine landsliding and their impact on flow
1037   behaviour: Geological Society, London, Special Publications, v. 477, p. SP477. 426.
1038   Hull, J., and Griffiths, C., 2002, Sequence stratigraphic evolution of the Albian to Recent section of
1039   the Dampier Sub-basin, North West Shelf, Australia: PhD thesis 1999. University of Adelaide,
1040   Australia.
1041   Ilg, B. R., Hemmings-Sykes, S., Nicol, A., Baur, J., Fohrmann, M., Funnell, R., and Milner, M., 2012,
1042   Normal faults and gas migration in an active plate boundary, southern Taranaki Basin,
1043   offshore New Zealand: AAPG bulletin, v. 96, no. 9, p. 1733-1756.
1044   Jackson, C. A., 2011, Three-dimensional seismic analysis of megaclast deformation within a mass
1045   transport deposit; implications for debris flow kinematics: Geology, v. 39, no. 3, p. 203-206.
1046   Keep, M., Powell, C. M., and Baillie, P., 1998, Neogene deformation of the North West Shelf,
1047   Australia.

1048   Kioka, A., Schwestermann, T., Moernaut, J., Ikehara, K., Kanamatsu, T., McHugh, C., dos Santos
1049   Ferreira, C., Wiemer, G., Haghipour, N., and Kopf, A., 2019, Megathrust earthquake drives
1050   drastic organic carbon supply to the hadal trench: Scientific reports, v. 9, no. 1, p. 1553.
1051   Kneller, B., Dykstra, M., Fairweather, L., and Milana, J. P., 2016, Mass-transport and slope
1052   accommodation: Implications for turbidite sandstone reservoirs: AAPG Bulletin, v. 100, no. 2,
1053   p. 213-235.
1054   Kvalstad, T. J., Andresen, L., Forsberg, C. F., Berg, K., Bryn, P., and Wangen, M., 2005, The Storegga
1055   slide: evaluation of triggering sources and slide mechanics: Marine and Petroleum Geology,
1056   v. 22, no. 1, p. 245-256.
1057   Lawrence, G. W., and Cartwright, J. A., 2010, The stratigraphic and geographic distribution of giant
1058   craters and remobilised sediment mounds on the mid Norway margin, and their relation to
1059   long term fluid flow: Marine and Petroleum Geology, v. 27, no. 4, p. 733-747.
1060   Li, S., Alves, T. M., Li, W., Wang, X., Rebesco, M., Li, J., Zhao, F., Yu, K., and Wu, S., 2022, Morphology
1061   and evolution of submarine canyons on the northwest South China Sea margin: Marine
1062   Geology, v. 443, p. 106695.
1063   Li, W., Alves, T. M., Wu, S., Völker, D., Zhao, F., Mi, L., and Kopf, A., 2015, Recurrent slope failure and
1064   submarine channel incision as key factors controlling reservoir potential in the South China
1065   Sea (Qiongdongnan Basin, South Hainan Island): Marine and Petroleum Geology, v. 64, p. 17-
1066   30.
1067   Li, W., Wu, S., Wang, X., Zhao, F., Wang, D., Mi, L., and Li, Q., Baiyun slide and its relation to fluid
1068   migration in the northern slope of Southern China Sea, *in* Proceedings Submarine mass
1069   movements and their consequences: 6th International Symposium2014, Springer, p. 105-
1070   115.
1071   Lintern, D. G., Mosher, D., Moscardelli, L., Bobrowsky, P., Campbell, C., Chaytor, J., Clague, J.,
1072   Georgiopoulou, A., Lajeunesse, P., and Normandeau, A., Subaqueous mass movements and
1073   their consequences: Assessing geohazards, environmental implications and economic
1074   significance of subaqueous landslides2019, Geological Society of London.
1075   Longley, I., Buessenschuett, C., Clydsdale, L., Cubitt, C., Davis, R., Johnson, M., Marshall, N., Murray,
1076   A., Somerville, R., and Spry, T., The North West Shelf of Australia—a Woodside perspective,
1077   *in* Proceedings The Sedimentary Basins of Western Australia 3: Proceedings of the Petroleum
1078   Exploration Society of Australia Symposium, Perth2002, Pet. Explor. Soc. of Aust. Perth, p.
1079   27-88.
1080   Masson, D., Harbitz, C., Wynn, R., Pedersen, G., and Løvholt, F., 2006, Submarine landslides:
1081   processes, triggers and hazard prediction: Philosophical Transactions of the Royal Society A:
1082   Mathematical, Physical and Engineering Sciences, v. 364, no. 1845, p. 2009-2039.
1083   Masson, D., Wynn, R., and Talling, P., 2010, Large landslides on passive continental margins:
1084   processes, hypotheses and outstanding questions, Submarine mass movements and their
1085   consequences, Springer, p. 153-165.
1086   Moernaut, J., and De Batist, M., 2011, Frontal emplacement and mobility of sublacustrine landslides:
1087   results from morphometric and seismostratigraphic analysis: Marine Geology, v. 285, no. 1-
1088   4, p. 29-45.
1089   Moscardelli, L., and Wood, L., 2016, Morphometry of mass-transport deposits as a predictive tool:
1090   Bulletin, v. 128, no. 1-2, p. 47-80.
1091   Moscardelli, L., Wood, L., and Mann, P., 2006, Mass-transport complexes and associated processes
1092   in the offshore area of Trinidad and Venezuela: AAPG bulletin, v. 90, no. 7, p. 1059-1088.
1093   Nardin, T. R., Hein, F., Gorsline, D. S., and Edwards, B., 1979, A review of mass movement processes
1094   sediment and acoustic characteristics, and contrasts in slope and base-of-slope systems
1095   versus canyon-fan-basin floor systems.
1096   Nelson, C. H., Escutia, C., Damuth, J. E., and Twichell, D., 2011, Interplay of mass-transport and
1097   turbidite-system deposits in different active tectonic and passive continental margin
1098   settings: external and local controlling factors: Sediment. Geol, v. 96, p. 39-66.

Nemec, W., 1990, Aspects of sediment movement on steep delta slopes: Coarse-grained deltas, v. 10, p. 29-73.

Nissen, S. E., Haskell, N. L., Steiner, C. T., and Coterill, K. L., 1999, Debris flow outrunner blocks, glide tracks, and pressure ridges identified on the Nigerian continental slope using 3-D seismic coherency: The Leading Edge, v. 18, no. 5, p. 595-599.

Nugraha, H. D., Jackson, C. A.-L., Johnson, H. D., and Hodgson, D. M., 2020, Lateral variability in strain along the toewall of a mass transport deposit: a case study from the Makassar Strait, offshore Indonesia: Journal of the Geological Society, v. 177, no. 6, p. 1261-1279.

Nugraha, H. D., Jackson, C. A.-L., Johnson, H. D., Hodgson, D. M., and Clare, M. A., 2022, Extreme erosion by submarine slides: Geology, v. 50, no. 10, p. 1130-1134.

Nugraha, H. D., Jackson, C. A. L., Johnson, H. D., Hodgson, D. M., and Reeve, M. T., 2018, Tectonic and oceanographic process interactions archived in Late Cretaceous to Present deep‐marine stratigraphy on the Exmouth Plateau, offshore NW Australia: Basin Research.

Nwoko, J., Kane, I., and Huuse, M., 2020, Megaclasts within mass-transport deposits: Their origin, characteristics and effect on substrates and succeeding flows: Geological Society, London, Special Publications, v. 500, no. 1, p. 515-530.

Omeru, T., and Cartwright, J. A., 2019, The efficacy of kinematic indicators in a complexly deformed mass transport deposit: insights from the deepwater Taranaki Basin, New Zealand: Marine and Petroleum Geology, v. 106, p. 74-87.

Paganoni, M., King, J. J., Foschi, M., Mellor-Jones, K., and Cartwright, J. A., 2019, A natural gas hydrate system on the Exmouth Plateau (NW shelf of Australia) sourced by thermogenic hydrocarbon leakage: Marine and Petroleum Geology, v. 99, p. 370-392.

Palmer-Julson, A., and Rack, F., 1992, The relationship between sediment fabric and planktonic microfossil taphonomy: how do plankton skeletons become pelagic ooze?: Palaios, p. 167-177.

Partyka, G., Gridley, J., and Lopez, J., 1999, Interpretational applications of spectral decomposition in reservoir characterization: The leading edge, v. 18, no. 3, p. 353-360.

Peakall, J., Best, J., Baas, J. H., Hodgson, D. M., Clare, M. A., Talling, P. J., Dorrell, R. M., and Lee, D. R., 2020, An integrated process‐based model of flutes and tool marks in deep‐water environments: Implications for palaeohydraulics, the Bouma sequence and hybrid event beds: Sedimentology, v. 67, no. 4, p. 1601-1666.

Piper, D., Pirmez, C., Manley, P., Long, D., Flood, R., Normark, W., and Showers, W., Mass-transport deposits of the Amazon Fan, *in* Proceedings PROCEEDINGS-OCEAN DRILLING PROGRAM SCIENTIFIC RESULTS1997, NATIONAL SCIENCE FOUNDATION, p. 109-146.

Piper, D. J., Cochonat, P., and Morrison, M. L., 1999, The sequence of events around the epicentre of the 1929 Grand Banks earthquake: initiation of debris flows and turbidity current inferred from sidescan sonar: Sedimentology, v. 46, no. 1, p. 79-97.

Pope, E. L., Talling, P. J., Carter, L., Clare, M. A., and Hunt, J. E., 2017, Damaging sediment density flows triggered by tropical cyclones: Earth and Planetary Science Letters, v. 458, p. 161-169.

Posamentier, H. W., and Kolla, V., 2003, Seismic geomorphology and stratigraphy of depositional elements in deep-water settings: Journal of sedimentary research, v. 73, no. 3, p. 367-388.

Posamentier, H. W., and Martinsen, O. J., 2011, The character and genesis of submarine mass-transport deposits: insights from outcrop and 3D seismic data: Mass-transport deposits in deepwater settings: Society for Sedimentary Geology (SEPM) Special Publication 96, p. 7-38.

Rack, F. R., Bryant, W. R., and Julson, A. P., 1993, Microfabric and physical properties of deep-sea high latitude carbonate oozes, Carbonate Microfabrics, Springer, p. 129-147.

Reis, A., Araújo, E., Silva, C., Cruz, A., Gorini, C., Droz, L., Migeon, S., Perovano, R., King, I., and Bache, F., 2016, Effects of a regional décollement level for gravity tectonics on late Neogene to recent large-scale slope instabilities in the Foz do Amazonas Basin, Brazil: Marine and Petroleum Geology, v. 75, p. 29-52.

1149 Rusconi, F. J., 2017, 3D seismic interpretation of a Plio-Pleistocene mass transport deposit in the
1150   deepwater Taranaki Basin of New Zealand, University of Arkansas.
1151 Safadi, M., Meilijson, A., and Makovsky, Y., 2017, Internal deformation of the southeast Levant
1152   margin through continued activity of buried mass transport deposits: Tectonics, v. 36, no. 3,
1153   p. 559-581.
1154 Sawyer, D. E., 2007, Lateral Variations in Core, Log, and Seismic Attributes of a Mass Transport
1155   Complex in the Ursa Region, IODP Expedition 308, Northern Gulf of Mexico.
1156 Sawyer, D. E., and DeVore, J. R., 2015, Elevated shear strength of sediments on active margins:
1157   Evidence for seismic strengthening: Geophysical Research Letters, v. 42, no. 23, p. 10,216-
1158   210,221.
1159 Sawyer, D. E., Flemings, P. B., Dugan, B., and Germaine, J. T., 2009, Retrogressive failures recorded in
1160   mass transport deposits in the Ursa Basin, Northern Gulf of Mexico: Journal of Geophysical
1161   Research: Solid Earth, v. 114, no. B10.
1162 Scarselli, N., McClay, K., and Elders, C., 2013, Submarine slide and slump complexes, Exmouth
1163   Plateau, NW Shelf of Australia, *in* Proceedings The Sedimentary Basins of Western Australia
1164   IV: Proceedings of the Petroleum Exploration Society of Australia Symposium, Perth,
1165   WA2013a, Volume 18.
1166 -, Submarine slide and slump complexes, Exmouth Plateau, NW Shelf of Australia, *in* Proceedings The
1167   Sedimentary Basins of Western Australia IV: Proceedings of the Petroleum Exploration
1168   Society of Australia Symposium, Perth, WA2013b.
1169 Schnyder, J. S., Eberli, G. P., Kirby, J. T., Shi, F., Tehranirad, B., Mulder, T., Ducassou, E., Hebbeln, D.,
1170   and Wintersteller, P., 2016, Tsunamis caused by submarine slope failures along western
1171   Great Bahama Bank: Scientific reports, v. 6, no. 1, p. 35925.
1172 Sharman, G. R., Graham, S. A., Masalimova, L. U., Shumaker, L. E., and King, P. R., 2015, Spatial
1173   patterns of deformation and paleoslope estimation within the marginal and central portions
1174   of a basin-floor mass-transport deposit, Taranaki Basin, New Zealand: Geosphere, v. 11, no.
1175   2, p. 266-306.
1176 Shipp, R. C., 2004, Physical Characteristics and Impact of Mass Transport Complexes on Deepwater
1177   Jetted Conductors and Suction Anchor Piles.
1178 Sobiesiak, M. S., Kneller, B., Alsop, G. I., and Milana, J. P., 2018, Styles of basal interaction beneath
1179   mass transport deposits: Marine and Petroleum Geology, v. 98, p. 629-639.
1180 Solheim, A., Berg, K., Forsberg, C., and Bryn, P., 2005, The Storegga Slide complex: repetitive large
1181   scale sliding with similar cause and development: Marine and Petroleum Geology, v. 22, no.
1182   1-2, p. 97-107.
1183 Steventon, M. J., Jackson, C. A. L., Hodgson, D. M., and Johnson, H. D., 2019, Strain analysis of a
1184   seismically imaged mass‐transport complex, offshore Uruguay: Basin Research, v. 31, no. 3,
1185   p. 600-620.
1186 Strout, J. M., and Tjelta, T. I., 2005, In situ pore pressures: What is their significance and how can
1187   they be reliably measured?: Marine and Petroleum Geology, v. 22, no. 1-2, p. 275-285.
1188 Sultan, N., Cochonat, P., Foucher, J., Mienert, J., Haflidason, H., and Sejrup, H., 2003, Effect of gas
1189   hydrates dissociation on seafloor slope stability, Submarine mass movements and their
1190   consequences, Springer, p. 103-111.
1191 Sun, Q., Alves, T. M., Lu, X., Chen, C., and Xie, X., 2018, True volumes of slope failure estimated from
1192   a Quaternary mass‐transport deposit in the northern South China Sea: Geophysical
1193   Research Letters, v. 45, no. 6, p. 2642-2651.
1194 Talling, P. J., CLARE, M. L., Urlaub, M., Pope, E., Hunt, J. E., and Watt, S. F., 2014, Large submarine
1195   landslides on continental slopes: geohazards, methane release, and climate change:
1196   Oceanography, v. 27, no. 2, p. 32-45.
1197 Tanaka, H., and Locat, J., 1999, A microstructural investigation of Osaka Bay clay: the impact of
1198   microfossils on its mechanical behaviour: Canadian Geotechnical Journal, v. 36, no. 3, p. 493-
1199   508.

1200   Ten Brink, U. S., Andrews, B. D., and Miller, N. C., 2016, Seismicity and sedimentation rate effects on
1201   submarine slope stability: Geology, v. 44, no. 7, p. 563-566.
1202   Tindale, K., Newell, N., Keall, J., Smith, N., Purcell, P., and Purcell, R., 1998, Structural evolution and
1203   charge history of the Exmouth Sub-basin, northern Carnarvon Basin, Western Australia: The
1204   sedimentary basins of Western Australia, v. 2.
1205   Urlaub, M., Talling, P. J., Zervos, A., and Masson, D., 2015, What causes large submarine landslides
1206   on low gradient (< 2°) continental slopes with slow (~ 0.15 m/kyr) sediment accumulation?:
1207   Journal of Geophysical Research: Solid Earth, v. 120, no. 10, p. 6722-6739.
1208   Van Bemmel, P. P., and Pepper, R. E., 2000, Seismic signal processing method and apparatus for
1209   generating a cube of variance values, Google Patents.
1210   Velayatham, T., Holford, S., Bunch, M., King, R., and Magee, C., 2019, 3D Seismic Analysis of Ancient
1211   Subsurface Fluid Flow in the Exmouth Plateau, Offshore Western Australia.
1212   Volpi, V., Camerlenghi, A., Hillenbrand, C. D., Rebesco, M., and Ivaldi, R., 2003, Effects of biogenic
1213   silica on sediment compaction and slope stability on the Pacific margin of the Antarctic
1214   Peninsula: Basin Research, v. 15, no. 3, p. 339-363.
1215   von Rad, U., Haq, B.U., et al., 1992, Proceedings of the Ocean Program, Scientific Results: Ocean
1216   Drilling Program, v. Leg 122.
1217   Ward, N. I., Alves, T. M., and Blenkinsop, T. G., 2018, Submarine sediment routing over a blocky
1218   mass‐transport deposit in the Espírito Santo Basin, SE Brazil: Basin Research, v. 30, no. 4,
1219   p. 816-834.
1220   Watkinson, I. M., and Hall, R., 2019, Impact of communal irrigation on the 2018 Palu earthquake-
1221   triggered landslides: Nature Geoscience, v. 12, no. 11, p. 940-945.
1222   Wu, N., Jackson, C. A.-L., Clare, M. A., Hodgson, D. M., Nugraha, H. D., Steventon, M. J., and Zhong,
1223   G., 2023, Diagenetic priming of submarine landslides in ooze-rich substrates: Geology, v. 51,
1224   no. 1, p. 85-90.
1225   Wu, N., Jackson, C. A.-L., Johnson, H. D., and Hodgson, D. M., 2021a, Lithological, petrophysical, and
1226   seal properties of mass-transport complexes, northern Gulf of Mexico: AAPG Bulletin, v. 105,
1227   no. 7, p. 1461-1489.
1228   Wu, N., Jackson, C. A. L., Johnson, H. D., Hodgson, D. M., Clare, M. A., Nugraha, H. D., and Li, W.,
1229   2021b, The formation and implications of giant blocks and fluid escape structures in
1230   submarine lateral spreads: Basin Research.
1231   Zhao, R., Chen, S., Olariu, C., Steel, R., Zhang, J., and Wang, H., 2019, A model for oblique accretion
1232   on the South China Sea margin; Red River (Song Hong) sediment transport into
1233   Qiongdongnan Basin since Upper Miocene: Marine Geology, v. 416, p. 106001.
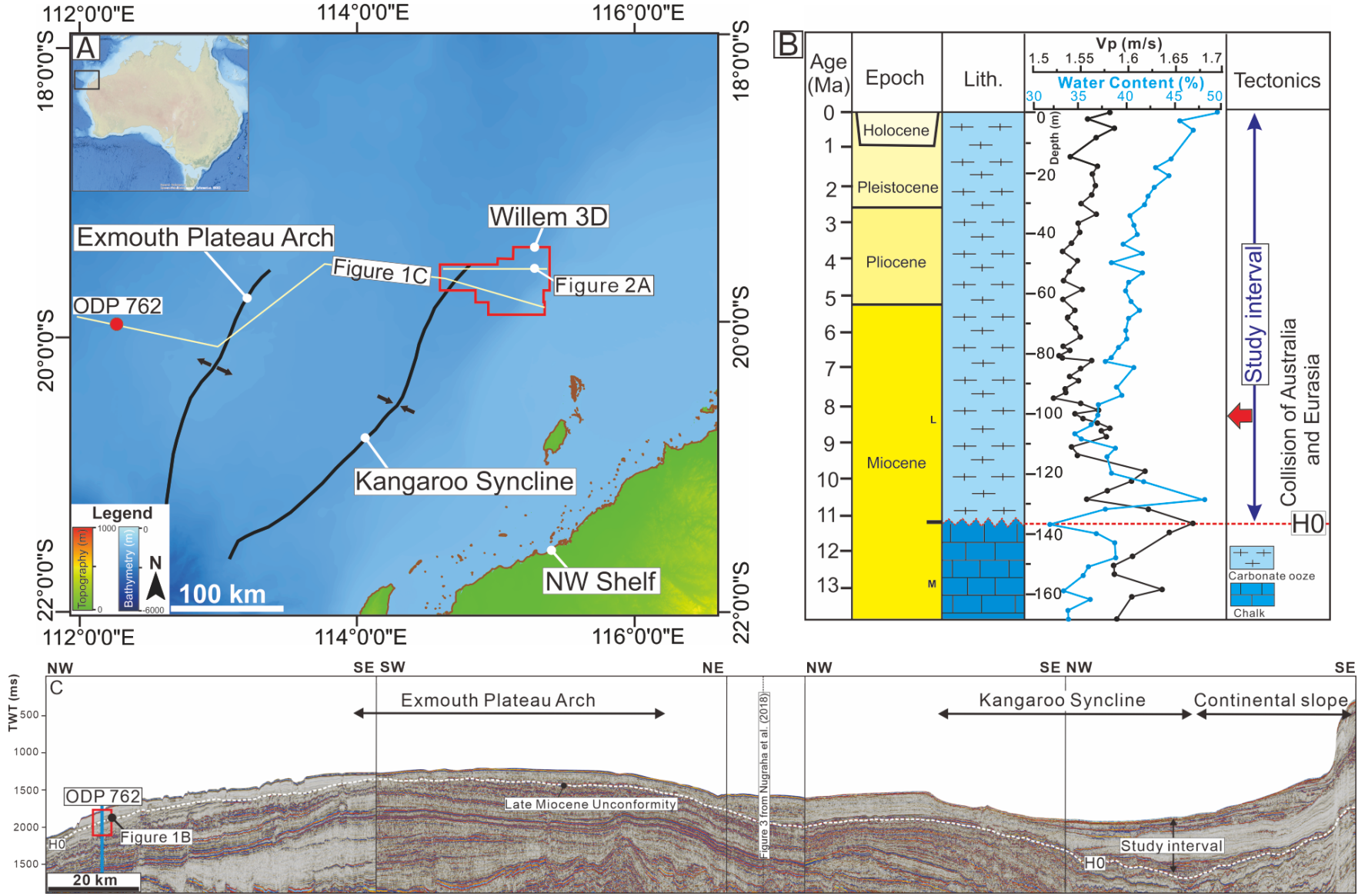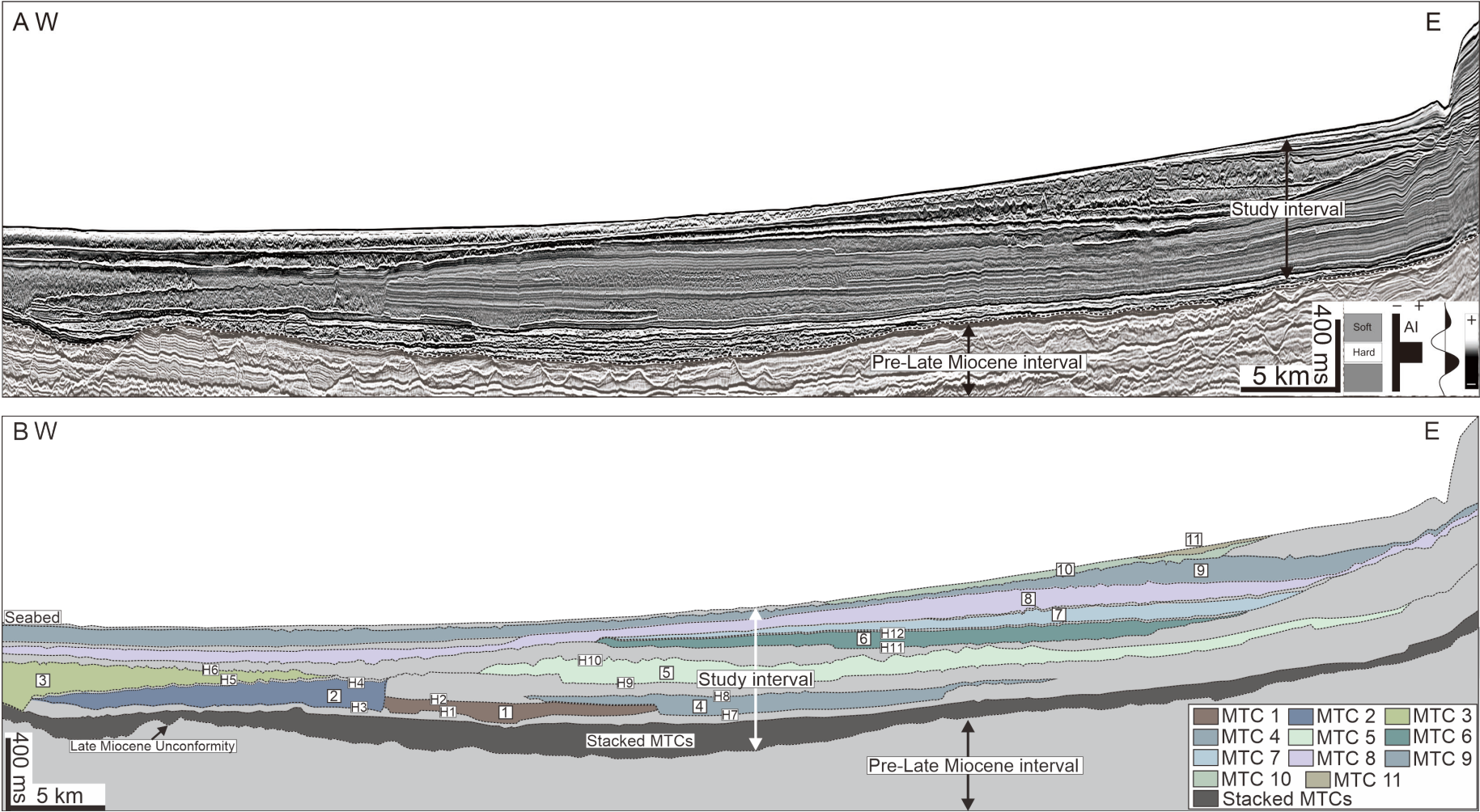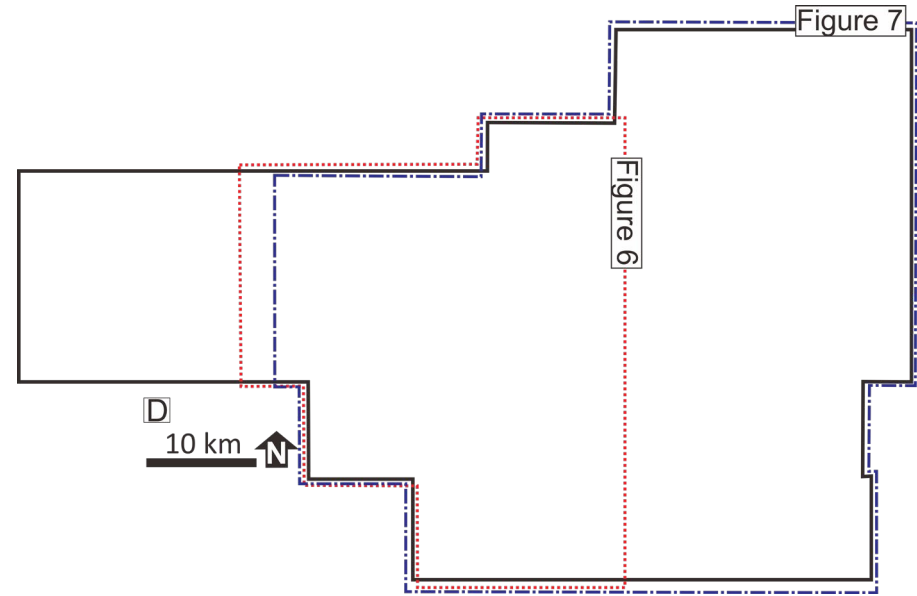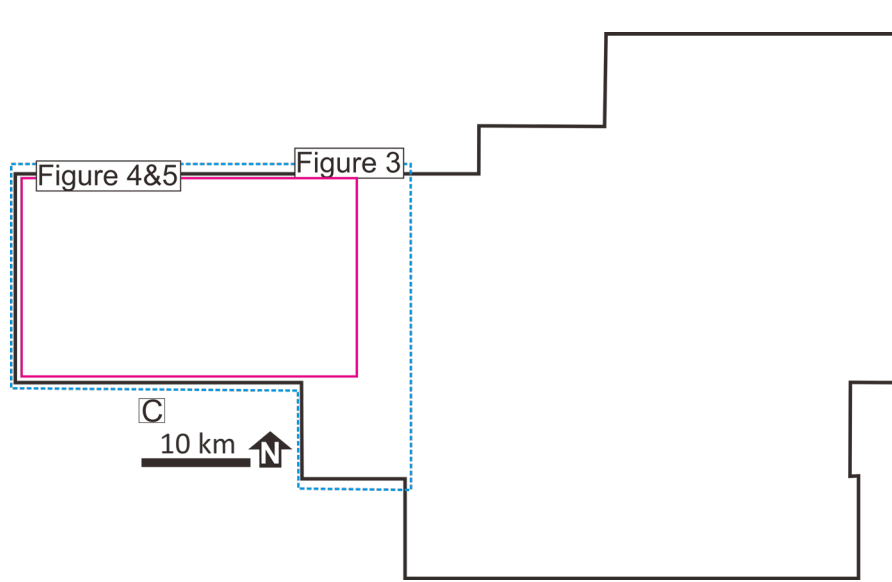
1234

Figure 1

Figure 2

Figure 4&5

Figure 3

C

10 km

N

Figure 7

Figure 6

D

10 km

N

Figure 3: MTC-1

Figure 3: MTC-1

Figure 4: MTC-2

Figure 4: MTC-2

Figure 5: MTC-3

A — Linear feature; Eastern boundary; Regularly spaced undulations; Low — Variance — High; 5 km

B — Scour; Pressure ridges; Figure 5E; Blocky area of MTC-2; MTC 3; Figure 5D; Transported block; Headwall scarp of MTC-2; 5 km; MTC-3; Undeformed strata

C — Eastern boundary of MTC-3; Thickness map of MTC-3; Thickness (TWT); 300 200 100 50; 5 km

D — SW; NE; H6; MTC-3; Scour; Scour; − +; AI; Soft; Hard; 100 (ms); 1000 m; H5

E — W; E; East boundary; Sediment drapes; Thrusts; MTC-3; MTC-2; Lateral spread; 100 (ms); 500 m

Figure 6: MTC-4

Figure 7_MTC-5
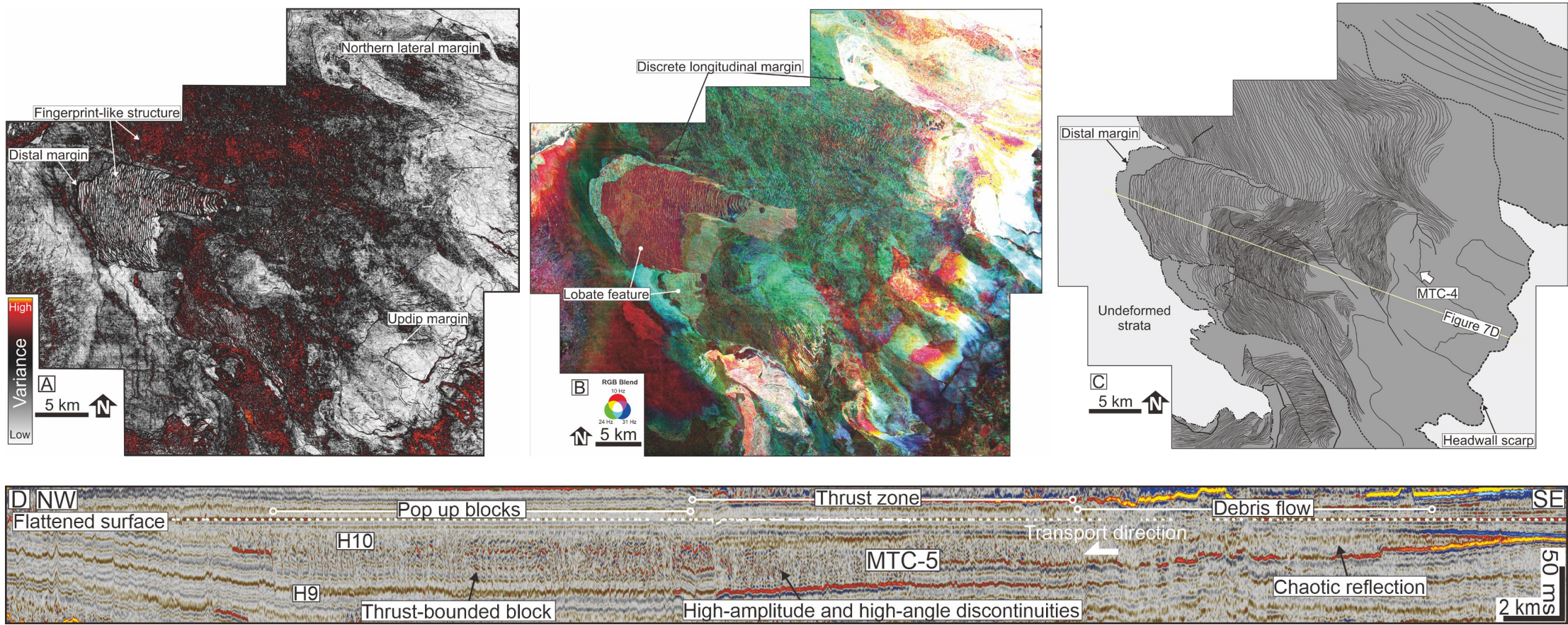
Figure 8_MTC-6&7

Figure 9_MTC-8

Depth map calculated on H15

A

Low Bathymetry (TWT) High

Lateral margin

Curvilinear lineation

Internal ramp

B Low Amplitude contrast High

10 km

Figure 11

Figure 10A

Groove

Groove

Figure 9D

Figure 10B

NW-SE trending lineation

MTC 8

C 10 km

MTC-8

Undeformed strata

200 150 100 50

D Thickness (ms)

10 km

Thickness map of MTC-8

E SW   NE

H16

H15

MTC-3   MTC-8

NW-SE trending internal ramp

MTC-2

Headwall scarp of MTC-2

Grooves

100 (ms)

1 km

Figure 10_MTC-8

Figure 11_MTC-8
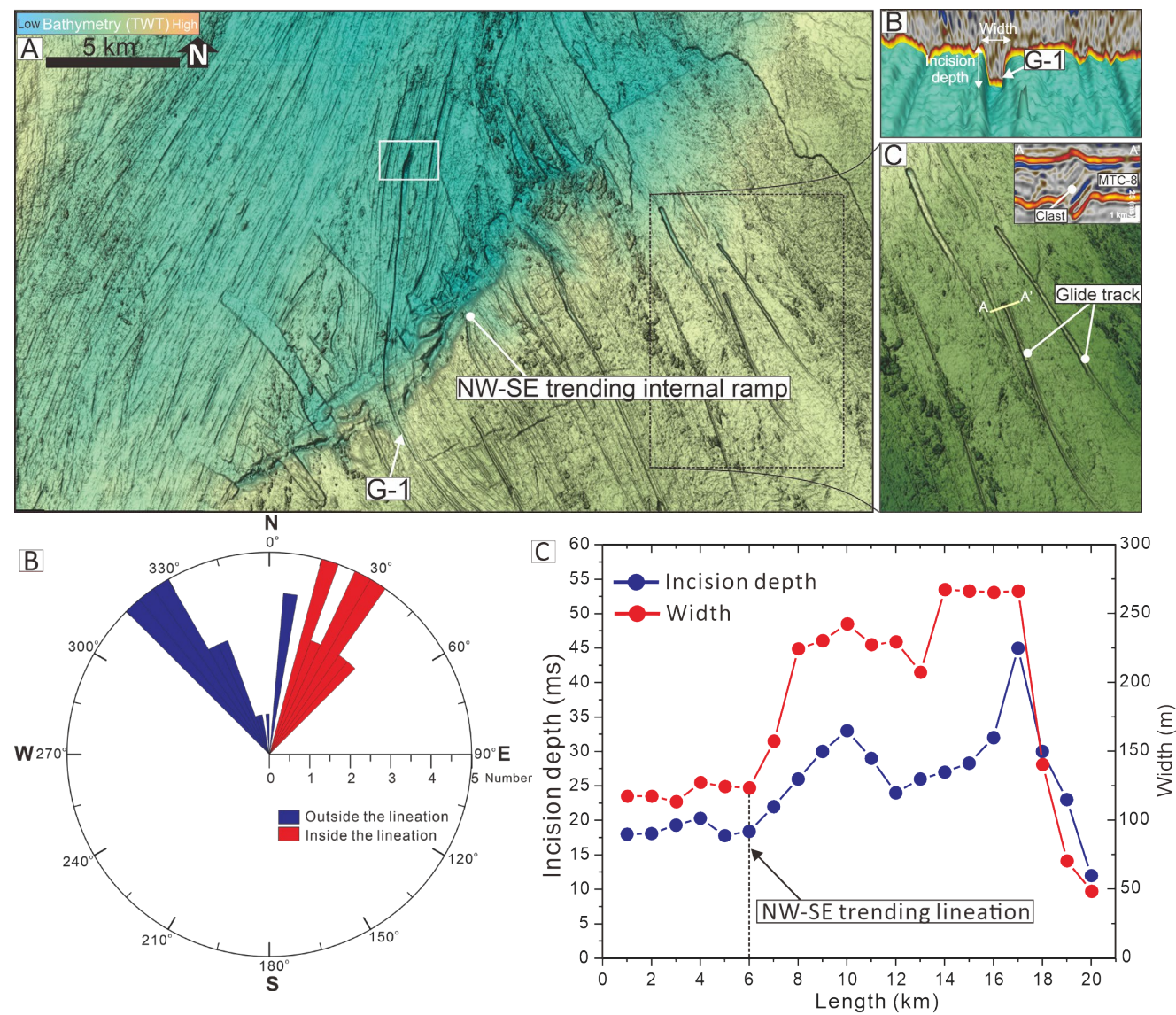
Figure 12_MTC-8; massive groove filed

Perspective 3D view of the same area as Figure 11A, rotated 180° clockwise

U-shaped erosion

MTC-8

NW-SE trending internal ramp

V-shaped erosion

Low Bathymetry (TWT) High
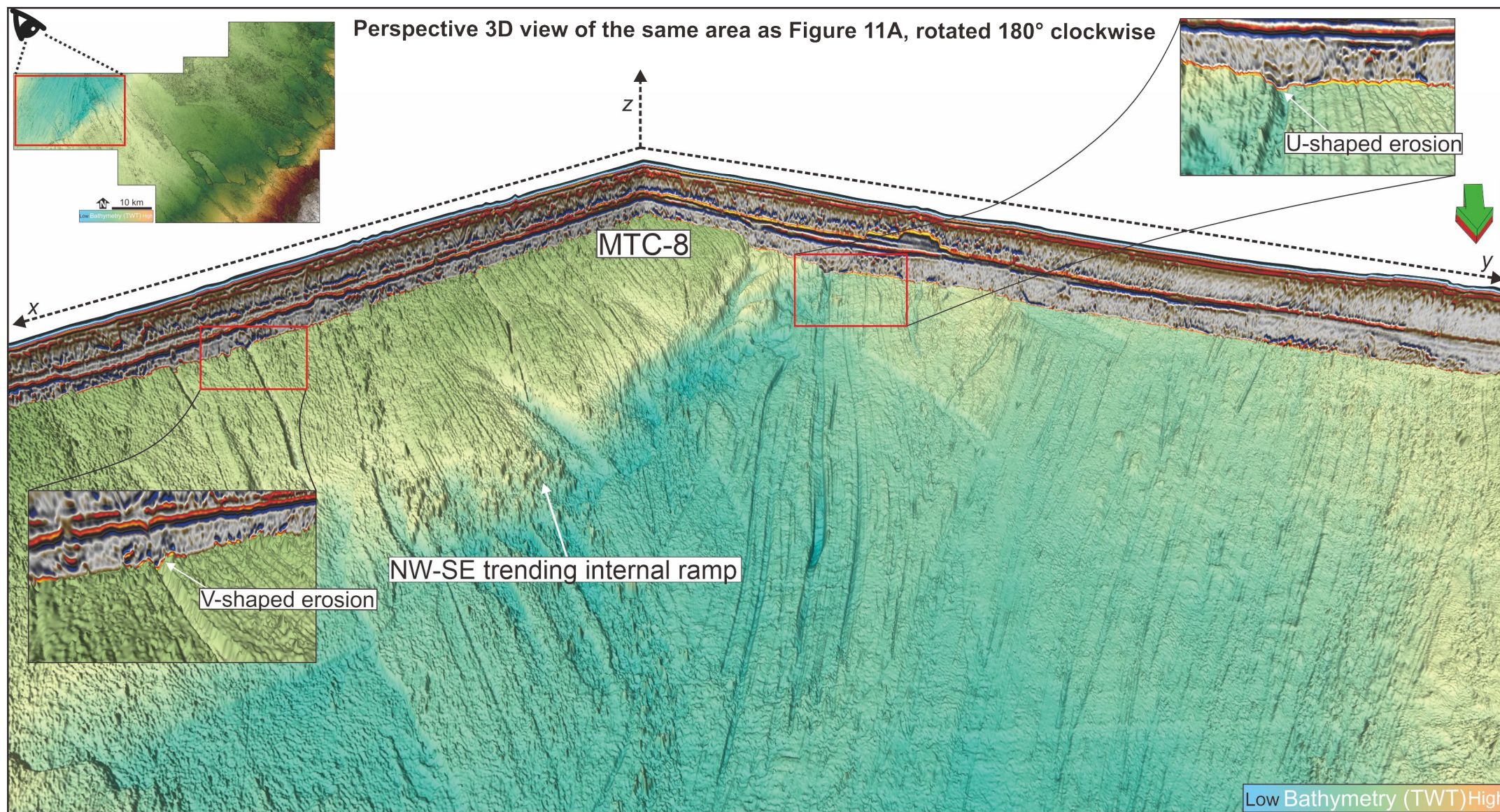
Figure 13_MTC-9
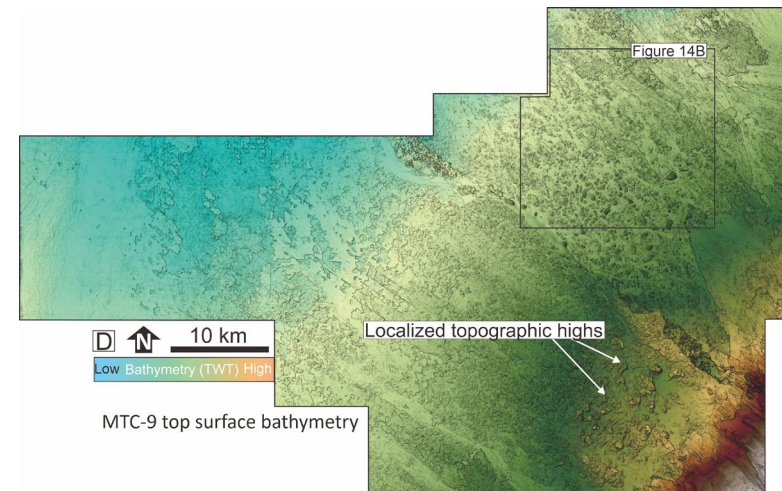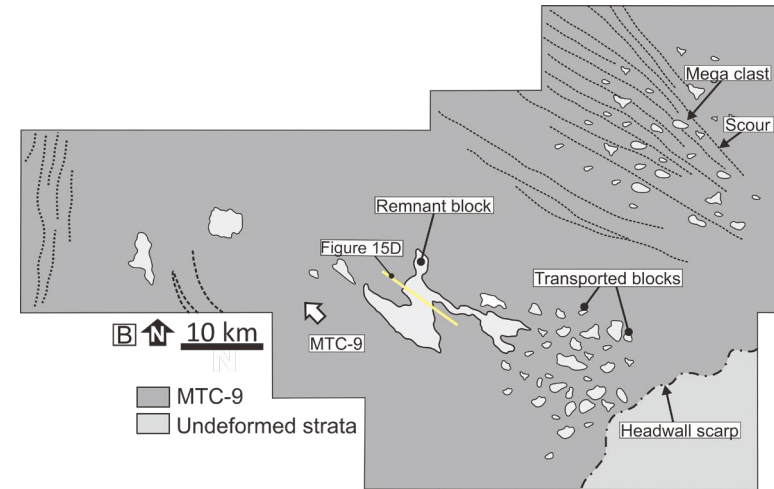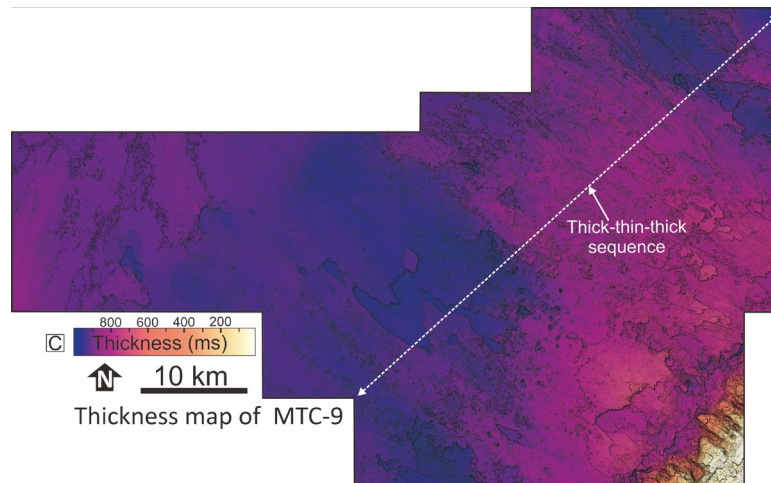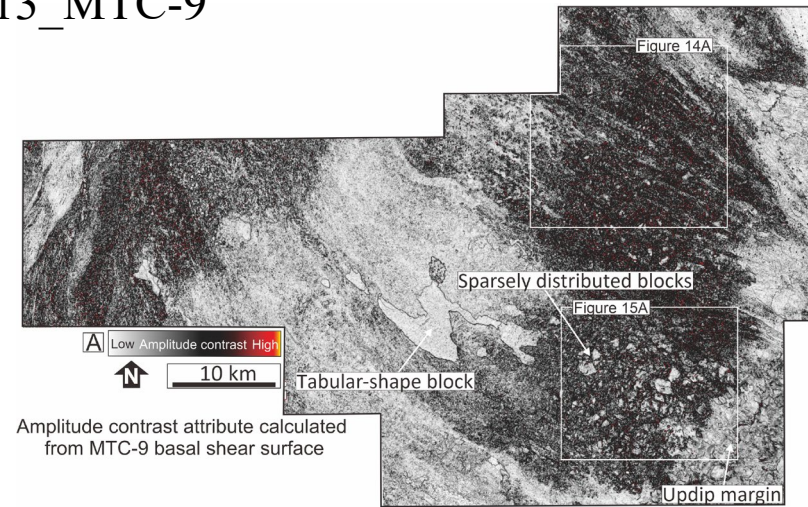
Figure 14

Figure 15_MTC-9 Blocks

A — Top surface of MTC-9. Transported block. Figure 15B. Figure 15C. 5 km. N. Low — Amplitude contrast — High.

B — NE. SW. Subsequent MTC thins and pinches out. Gentle stoss side. Steep lee side. c. 120m. c. 270 m. Seismic onlap. H18. MTC-9. H17. 100ms. 1 km.

C — NE. SW. Seabed topography created by blocks. H18. MTC-9. H17. Deformed to chaotic seismic reflections. 100ms. 1 km.

D — SW. NE. H18. MTC-9. H17. Remnant block. Steep flank. 100ms. 500 ms.

Figure 16; MTC-10&11

Figure 17

Figure 18

Figure 19